APL Photonics

TUTORIAL | NOVEMBER 07 2025

Gradient metasurfaces for integrated optics, plasmonics, and optoelectronics

Maliheh A. Roueini ; Roberto Paiella

APL Photonics 10, 111102 (2025)
https://doi.org/10.1063/5.0284959

AIP Publishing

Gradient metasurfaces for integrated optics, plasmonics, and optoelectronics

Cite as: APL Photon. 10, 111102 (2025); doi: 10.1063/5.0284959
Submitted: 11 June 2025 • Accepted: 15 October 2025 •
Published Online: 7 November 2025

Maliheh A. Roueini and Roberto Paiella[a)]

AFFILIATIONS

Department of Electrical and Computer Engineering and Photonics Center, Boston University, 8 Saint Mary's Street, Boston, Massachusetts 02215, USA

[a)]Author to whom correspondence should be addressed: rpaiella@bu.edu

ABSTRACT

Gradient metasurfaces provide a well-established platform for the wavefront and polarization control of light propagating in free space. More recent studies have also focused on their integration with plasmonic and dielectric waveguides and optoelectronic devices such as light emitters and photodetectors. In this context, metasurfaces can be used to interface guided modes with free-space radiation, for example, to enforce the selective input coupling or detection of light with prescribed characteristics (in terms of direction of propagation, state of polarization, orbital angular momentum, etc.) or to manipulate the properties of the out-coupled or emitted light according to a desired system operation. These functionalities, which normally involve complex combinations of bulky optical elements, have important applications in multiple areas of high technological significance, from optical interconnects to microdisplays and multifunctional image sensors. Here, we provide a tutorial overview of this field of research, including a description of the basic building blocks (meta-atoms) used in integrated gradient metasurfaces, a review of the main capabilities reported to date, and an outlook on future directions of study and technological prospects.

I. INTRODUCTION

Metasurface flat optics is a relatively recent branch of research and development in photonics that is currently in the process of revolutionizing the optical component landscape.[1–5] Broadly speaking, a metasurface is a planar array of metallic or dielectric nanoparticles (NPs) featuring subwavelength nearest-neighbor separations, designed to control the flow of light on a point-by-point basis. In phase gradient metasurfaces, each NP introduces a predetermined phase shift in the locally incident optical field upon transmission or reflection, while at the same time adding minimal propagation losses. Depending on the transmission or reflection phase profile encoded across the entire array, the metasurface can therefore perform a wide range of wavefront shaping functionalities, such as beam deflection, focusing, image formation, holography, and the generation of light with orbital angular momentum (OAM). The metasurface response can be designed to be uniform with respect to polarization or, alternatively, anisotropic NP arrays can be constructed to impart different phase profiles on orthogonal polarization components.[6,7] Similarly, the spectral response can be tailored to achieve achromatic wavefront control across a desired bandwidth or to enhance dispersion for wavelength-multiplexed operation, depending on the intended application.[8]

The same wavefront shaping functionalities can also be implemented with traditional refractive or diffractive optical components, e.g., prisms or gratings for beam deflection, lenses for focusing and image formation, wave plates for polarization control, and so forth. However, metasurfaces offer a combination of several intrinsic advantages that have fueled explosive growth in their development over the past decade. First, as implied by their "surface" designation, they are ultrathin (typically several tens to a few hundred nanometers), which makes them uniquely suited for system applications where miniaturization, low weight, and portability are essential. This advantage is further compounded by their extreme design flexibility for multifunctional operation (e.g., to project different polarization components of an incident wave onto different regions of an image sensor array for polarization vision). Such capabilities are again already available with traditional optics but require cascaded combinations of bulk optical elements of increasing size and complexity with increasing functionality, which often makes them

impractical. In addition, by virtue of their "flat" nature, metasurfaces are suitable for large-scale manufacturing in a foundry, which can be quite inexpensive, especially if CMOS compatible materials are involved. In contrast, even a component as mature and well established as a lens can still add significant manufacturing costs to its intended application due to the complexity of preparing optical-quality curved surfaces. Importantly, even though the metasurface building blocks (meta-atoms) have highly subwavelength lateral dimensions, their accurate fabrication over a sufficiently large area is well within the capabilities of state-of-the-art nanofabrication tools such as electron-beam and deep UV lithography. In fact, while some of the underlying ideas were already known from millimeter-wave and antenna electromagnetics,[9] the widespread emergence of metasurface flat optics took place in parallel with suitable fabrication tools becoming widely available in research labs worldwide.

Traditional metasurface devices are free-standing plates used to shape the wavefronts and/or polarization distribution of incident light propagating in free space [Fig. 1(a)]. For example, metalenses are designed to introduce a transmission phase delay that decreases with increasing distance from their optical axis according to the lens equation. More recently, extensive research efforts have also focused on the direct integration of metasurfaces within waveguided and active optoelectronic devices, particularly light emitters and photodetectors.[10–14] In this case, the optical field transformation implemented by the metasurface amounts to matching the guided modes supported by the underlying device to incoming or outgoing radiation with prescribed properties (e.g., in terms of direction of propagation, state of polarization, OAM, etc.) [Figs. 1(b) and 1(c)]. This configuration therefore adds a new level of miniaturization for optical system design, where multiple bulk elements are normally used to interface waveguides, light sources, and photodetectors with free-space radiation, either to manipulate the properties of the out-coupled or emitted light according to a desired system operation or to enable the selective in-coupling or detection of light with desired properties. Furthermore, since typical optoelectronic devices are also based on a planar form factor, the metasurface integration can be quite straightforward and, depending on the materials involved, can even be included seamlessly as an additional step in the device fabrication flow at the foundry level.

The present tutorial is focused on this emerging area of research. It should be noted that the integration of NP arrays near the active layers of optoelectronic devices has a rich history of scientific and technological explorations, for example, involving dispersion engineering with photonic crystals[15] or field enhancement effects near plasmonic nanostructures.[16] While these systems are also sometimes referred to as metasurfaces (in the broad sense of two-dimensional artificially engineered materials with properties that go beyond what is commonly found in nature), here we predominantly consider gradient metasurfaces designed to tailor the spatial distribution of phase and polarization point-by-point according to the design of the different meta-atoms. In the spirit of a tutorial, we begin by describing the operation of the basic building blocks of these metasurfaces, including gap-plasmon nanoantennas, dielectric NPs, and unit cells based on the Pancharatnam–Berry (PB) phase (Sec. II). The use of arrays of these building blocks to couple light in and out of plasmonic and dielectric waveguides is presented in Sec. III. In Secs. IV and V, we then review recent work where the meta-atoms are assembled on the active surfaces of light emitting devices and photodetectors, respectively, to enable new integrated-device capabilities across different degrees of freedom. The common thread of all configurations described in Secs. III–V is the use of metasurfaces to couple free-space radiation with guided electromagnetic modes (in waveguides, light emitters, or photodetectors). Finally, we conclude the tutorial in Sec. VI with a discussion of ongoing challenges and potential opportunities for a lasting technological impact.

II. BASIC BUILDING BLOCKS

A phase gradient metasurface is functionally equivalent to a planar interface that imparts a predetermined transverse-position-dependent phase shift $\varphi(x, y)$ on incident light upon reflection or transmission, without at the same time affecting the intensity distribution. The target phase response $\varphi(x, y)$ and operating wavelengths are determined by the intended application, and multiple examples are presented in Secs. III–V. In addition, depending on the application, the desired phase response may be isotropic, or two different phase profiles may be encoded on two prescribed orthogonal states of polarization. Practical implementations involve a dense array of NPs on a planar substrate, where the unit cell centered at any location (x_n, y_m) is designed to provide a reflection or transmission phase equal to the local value $\varphi(x_n, y_m)$ of the target phase profile. For optimal utilization of the substrate area, the NPs are typically distributed in a periodic lattice, with sufficiently small periods Λ to ensure that all nonzero diffraction orders are evanescent to avoid radiative diffraction losses. If the metasurface is intended to operate with light incident along arbitrary directions, this condition requires the period to be smaller than half the wavelength in both surrounding media. All the NPs are usually patterned from a single metallic or dielectric film deposited on the substrate, and as a result, they are

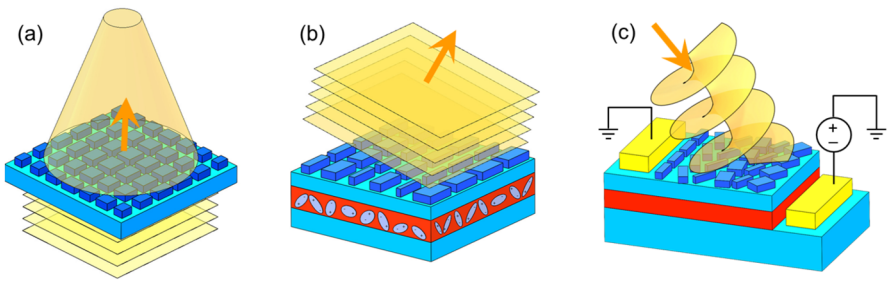

FIG. 1. Representative metasurface devices. (a) Free-space metalens. (b) Metasurface-integrated directional light emitter. (c) Metasurface-integrated wavefront-sensitive photodetector.

required to have the same height and material composition. Their shape, lateral dimensions, and orientation on the plane of the substrate, on the other hand, can be varied at will across the different unit cells, within the constraints of the available space and existing nanofabrication capabilities. The key requirement for any metasurface building block then is the ability to tune its transmission or reflection phase across the full 2π range by varying these geometrical parameters to allow for the implementation of any desired phase response. Different types of building blocks are described below, together with their respective advantages and limitations. The main figures of merit of the resulting arrays are their absorption and scattering losses, as well as the fidelity of the imparted phase shifts to the target profiles.

A highly effective solution for infrared device applications is the gap-plasmon metasurface architecture[17] illustrated schematically in Fig. 2(a), where each unit cell contains a metallic NP of suitably designed shape (e.g., rectangular in the figure). These NPs support localized plasmonic resonances, where the free electrons within the metal oscillate periodically under the driving action of the incident optical field and the restoring force provided by the resulting uncompensated ions on the NP sidewalls. As in a simple harmonic oscillator, the resonance frequency of these dipolar excitations is determined by the restoring force, which in turn depends on the NP geometry—e.g., it decreases with increasing separation between the NP sidewalls perpendicular to the driving electric field, leading to a (polarization dependent) red shift in the resonance wavelength. These resonances produce an absorption peak (related to ohmic damping of the electronic oscillations) as well as phase dispersion in the NP spectral response. At near-infrared wavelengths, where the imaginary permittivity of noble metals is relatively small, the resulting absorption losses can be quite manageable. The phase dispersion can be exploited to control the NP reflection or transmission phase $\varphi(x_n, y_m)$ at any target operation wavelength λ by varying the NP dimensions to tune its resonance and, therefore, shift its spectral response. Importantly, however, due to the dipolar nature of these excitations, their phase excursion across the spectral linewidth is fundamentally limited to a maximum value of π. In gap-plasmon metasurfaces, this limitation is overcome by placing the NPs on a metallic ground plane with a subwavelength dielectric spacer in between [Fig. 2(a)]. In this configuration, the oscillating electron gas in each NP produces an oscillating image charge in the underlying metal film, which adds up to the optical response, effectively doubling the phase excursion. This conclusion can be validated with a general model based on coupled-mode theory.[18] To illustrate, in Fig. 2(b), we show the reflection phase of the Au/SiO_2/Au meta-atom of Fig. 2(a), computed by finite difference time domain (FDTD) simulations as a function of NP lateral dimensions L_x and L_y. In these simulations, the incident light has a 1550-nm wavelength and linear polarization along the x direction (the same results with the horizontal and vertical axes interchanged apply for y-polarized light). The key point to observe in this figure is the large overall phase variations, close to the full 2π range. At the same time, the calculated reflection amplitudes (not shown) indicate relatively low absorption losses, with an average reflection coefficient over all simulated values of L_x and L_y of about 91%.

The configuration just described is restricted to operation in the reflection mode (due to the presence of the metallic backplane) and cannot be extended to the visible range, where plasmonic absorption becomes prohibitively large. For example, similar calculations show that, at a representative visible wavelength of 550 nm, resonant absorption in similar plasmonic meta-atoms can attenuate the incident light by over an order of magnitude. Both limitations can be avoided using high-index dielectric NPs on a transparent substrate [Fig. 2(c)]. Under illumination from either the air above or the substrate, each NP behaves like a single-mode nano-waveguide (terminated into a low-quality-factor Fabry–Perot cavity), where

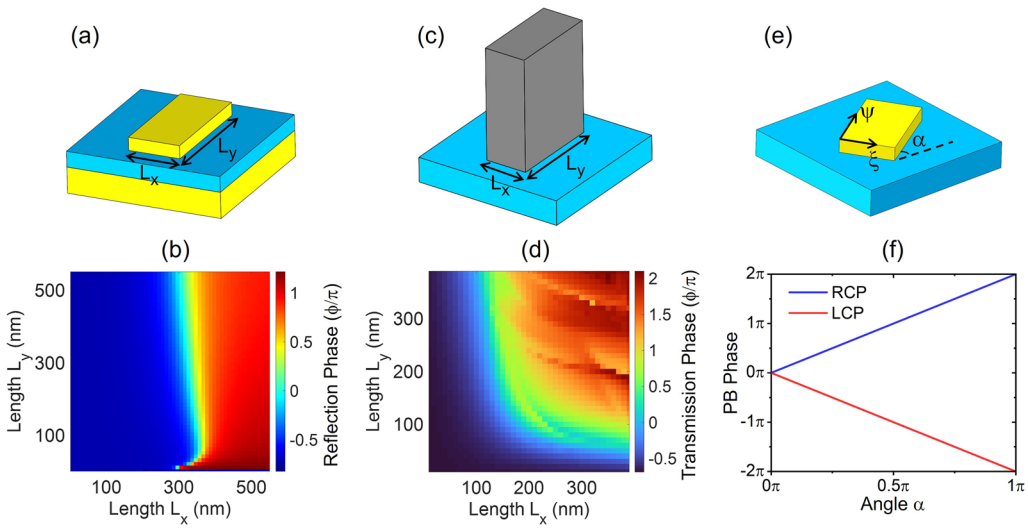

FIG. 2. Basic unit-cell architectures used in metasurface devices. (a), (b) Schematic illustration (a) and reflection phase response at λ = 1550 nm (b) of a Au/SiO_2/Au gap-plasmon meta-atom. (c) and (d) Schematic illustration (c) and transmission phase response at λ = 550 nm (d) of a TiO_2 NP on a SiO_2 substrate. (e) and (f) Schematic illustration (e) and transmission phase vs NP orientation angle under circularly polarized illumination (f) of a PB-metasurface unit cell.

light propagates along the vertical (out-of-plane) direction.[19,20] The transmission phase $\varphi(x_n,y_m)$ of each meta-atom is then determined by the propagation constant β of the guided mode multiplied by the waveguide length (the NP height h). The propagation constant in turn depends on the NP lateral dimensions, which control the degree of confinement of the guided mode in the high-index core (the larger the NP, the more strongly confined the mode and, therefore, the larger β). Once again, different phase responses can also be produced for different states of polarization. For example, in the rectangular NPs of Fig. 2(c), the polarization eigenstates are linear along the x and y directions, and their respective propagation constants (for fixed L_x and L_y) are different due to the different boundary conditions experienced by parallel and perpendicular optical-field components. The calculated x-polarized transmission phase of meta-atoms based on this geometry, consisting of 600-nm-tall TiO_2 NPs on a SiO_2 substrate, is plotted in Fig. 2(d) vs lateral dimensions at $\lambda = 550$ nm. The total phase variations in this plot are about 2.7π, while negligible absorption losses are correspondingly computed due to the transparent nature of the constituent dielectric materials. In principle, similar meta-atoms could be employed for operation at longer (infrared) wavelengths, although the need for proportionally taller NPs can add significant fabrication complexity. All-dielectric phase gradient metasurfaces can also be implemented with suitably designed Mie-type NPs featuring spectrally overlapping electric and magnetic dipolar scattering resonances.[21,22] As in the plasmonic NPs described earlier, the spectral position of these resonances can be tuned by design by varying the NP shape and dimensions, which in turn allows controlling the scattering phase at any desired wavelength near resonance.

An alternative metasurface platform relies on the PB, or geometric, phase of anisotropic NPs (either metallic or dielectric) under circularly polarized illumination.[23,24] To illustrate, in Fig. 2(e), we consider again a simple rectangular NP, but now rotated by an angle α with respect to the axes of the metasurface array. The optical response of this meta-atom is analogous to that of a wave plate with fast and slow axes parallel to the sides of the NP [the ξ and ψ directions in Fig. 2(e)]. The Jones matrix that describes transmission through this meta-atom in the right- and left-circularly polarized (RCP and LCP) basis can then be derived as follows:

$$M = \frac{1}{2}\begin{bmatrix} t_\xi + t_\psi & (t_\xi - t_\psi)e^{-i2\alpha} \\ (t_\xi - t_\psi)e^{i2\alpha} & t_\xi + t_\psi \end{bmatrix}, \quad (1)$$

where t_ξ and t_ψ are the amplitude transmission coefficients for light with linear polarization along the ξ and ψ directions. A similar expression applies for the reflection Jones matrix. If the NPs are designed so that $|t_\xi + t_\psi| \ll |t_\xi - t_\psi|$, most of the incident RCP light experiences a reversal in the direction of field rotation accompanied by a total phase shift $\varphi_{tot} = \arg\{t_\xi - t_\psi\} + 2\alpha$. Similarly, the LCP component is predominantly converted into RCP light with the same NP resonance or propagation phase $\varphi_{NP} = \arg\{t_\xi - t_\psi\}$ but equal and opposite PB phase $\varphi_{PB} = -2\alpha$ [Fig. 2(f)]. Any desired transmission phase profile $\varphi(x,y)$ can then be imparted on either circular polarization component using an array of anisotropic NPs of identical shape and dimensions, each rotated by the required angle to achieve the local phase value $\varphi(x_n, y_m)$. At the same time, the opposite circular polarization component is transmitted through the same metasurface with the conjugate phase profile $-\varphi(x, y)$ (up to a position-independent phase constant). Additional design flexibility can be achieved by varying the size and shape, in addition to the orientation, of the individual NPs to control the phase shifts $\arg\{t_\xi\}$ and $\arg\{t_\psi\}$. This approach allows for the independent wavefront manipulation of the incident RCP and LCP components, or more generally of any two orthogonal polarizations.[7] Alternatively, it could be applied to a single circular polarization channel to simultaneously control (in addition to the phase) the local amplitude of the cross-polarized transmitted light,[25] which is proportional to $|t_\xi - t_\psi|$ according to Eq. (1). It should also be noted that, unlike the resonance or propagation phase of plasmonic or dielectric NPs, the PB phase is completely constant with wavelength, which can be exploited to separately control phase and dispersion for the design of broadband achromatic metasurface devices.[8]

All the metasurfaces reviewed in this section could also be described as a natural evolution of diffractive optical elements (DOEs)—i.e., microstructured surfaces (including binary, multilevel, and blazed elements, holographic plates, and spatial light modulators) designed to manipulate light through diffraction and interference.[26] The key difference is provided by the subwavelength dimensions of the metasurface building blocks, which allow for arbitrary and continuous wavefront shaping as well as multifunctional phase, amplitude, and polarization control capabilities that are not readily available with DOEs. Finally, it should also be mentioned that more complex multifunctional metasurface architectures can be developed using inverse design strategies such as topology optimization, machine learning, and physics informed neural networks. With this approach, the desired metasurface functionality is specified as an objective function, and the optimal geometry (possibly involving aperiodic arrays of arbitrarily shaped NPs) is then determined through a computational optimization task subject to predetermined constraints. Recent advances in this emerging field of study are reviewed, e.g., in Refs. 27 and 28.

III. WAVEGUIDE COUPLERS

The key functionality of metasurfaces for integrated optoelectronics is the ability to interface free-space radiation with waveguided modes. This task is traditionally performed by launching or collecting light through the waveguide input or output facets, or vertically with the assistance of a diffraction grating on the waveguide top surface. The former approach is limited by stringent alignment requirements, especially when the guided modes are tightly confined or in complex photonic integrated circuits with multiple input/output ports. The latter approach, illustrated in Fig. 3, employs diffraction to compensate for the phase mismatch caused by the different in-plane wavevectors of free-space radiation ($k_{||} = 2\pi \sin\theta/\lambda$, where θ is the angle of incidence) and guided modes ($\beta = 2\pi n_{eff}/\lambda$, where $n_{eff} > 1$ is the mode effective index). Specifically, diffraction in the configuration of Fig. 3(a) can shift the in-plane (x) component of the incident wavevector by any integral multiple of the grating wavevector $2\pi/\Lambda$, where Λ is the grating period. Light can, therefore, be coupled into the guided mode by any incoming wave with wavelength λ and angle of incidence θ that satisfy the phase-matching condition $2\pi \sin\theta/\lambda + 2q\pi/\Lambda = 2\pi n_{eff}/\lambda$ for some integral diffraction order q [e.g., q = 1 in Fig. 3(b)] (and similarly for waveguide outcoupling). The efficiency of this process depends on the refractive-index

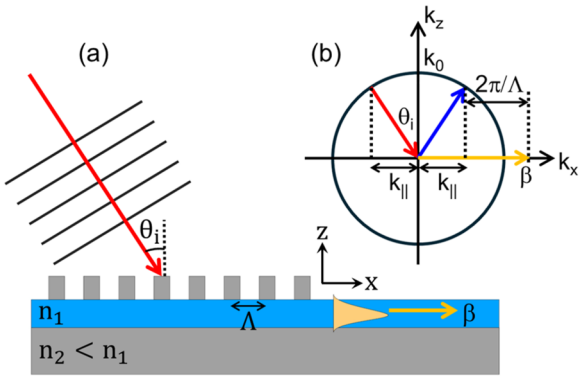

FIG. 3. Waveguide input coupling with a diffraction grating. (a) Schematic illustration. (b) Phase-matching diagram showing the excitation of a mode of wavevector β by free-space radiation of wavelength λ (wavenumber $k_0 = 2\pi/\lambda$) and angle of incidence θ through positive-first-order diffraction.

contrast of the grating and its detailed shape, which determines the relative strength of the different diffraction orders.

The same phase matching can also be achieved with a metasurface integrated over the waveguide and designed to introduce a linear phase profile with a suitable slope, i.e., $\varphi(x, y) = 2\pi(n_{eff} - \sin\theta)x/\lambda$ if the direction of propagation of the guided mode ($\hat{x}$) lies on the plane of incidence as in Fig. 3(b). Compared to diffraction gratings, however, metasurfaces offer several important advantages. First, while a grating generally scatters light into multiple diffraction orders (only one of which is phase-matched to the target guided mode), a metasurface can impart the required phase profile on the entire scattered wave, therefore allowing for higher coupling efficiency. In this respect, a linear-phase-gradient metasurface is thus equivalent to a blazed diffraction grating, but with a significantly simpler fabrication process due to its uniform thickness. Second, metasurface dispersion engineering[8] can be employed to enforce the required phase profiles for efficient waveguide coupling across a broad spectral region, whereas diffraction grating couplers are limited to a narrow, fixed operation bandwidth. Finally, the enhanced design flexibility of metasurfaces can be further exploited to selectively phase-match a guided mode with free-space radiation of any desired polarization or wavefront distribution. Specifically, if the meta-atoms are selected to produce, in addition to the outcoupling linear phase gradient, an arbitrary phase profile $\Delta\varphi(x, y)$, the same phase distribution will be encoded in the waveguide output light. For example, a converging beam focused at a distance f from the metasurface is obtained with $\Delta\varphi(x,y) = 2\pi\left(f - \sqrt{x^2 + y^2 + f^2}\right)/\lambda$ (the lens phase profile). Similarly, if the same metasurface is used for input coupling, the target guided mode will only be excited by incident light with the conjugate phase distribution $-\Delta\varphi(x, y)$ (e.g., diverging toward the metasurface from the same focal point in the example mentioned earlier).

These ideas have been applied extensively to the excitation of surface plasmon polaritons (SPPs) at metal–dielectric interfaces.[29–37] By virtue of their strong optical-field confinement, these guided waves are promising for multiple applications ranging from biochemical sensing[38] to large-scale photonic integrated circuits.[39] At the same time, however, their highly subwavelength nature also makes them particularly challenging to interface with free-space

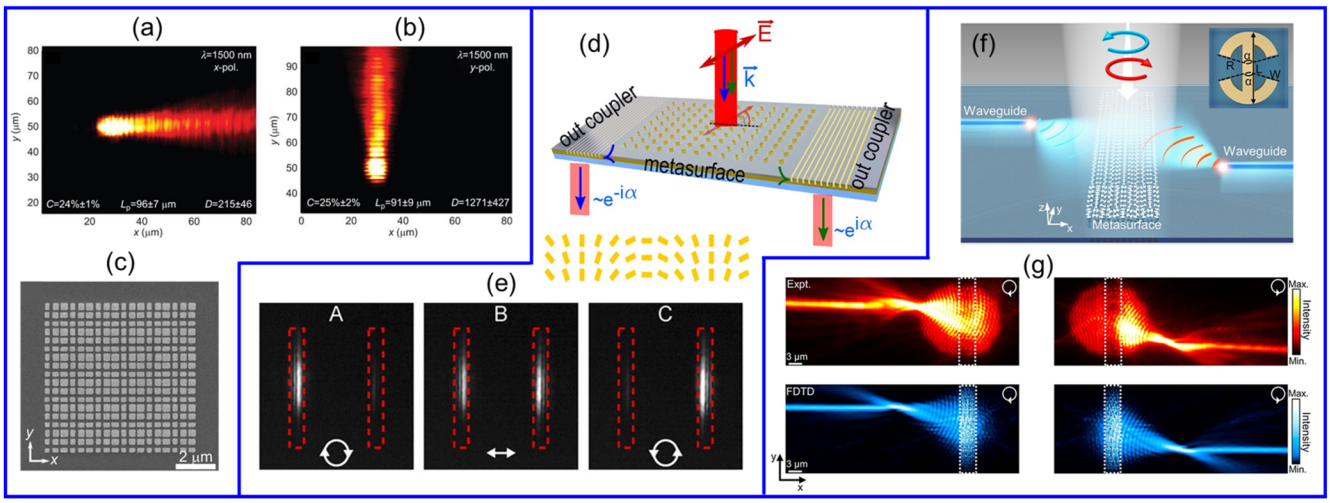

FIG. 4. Metasurface plasmonic waveguide couplers. (a)–(c) Linear-polarization-dependent unidirectional excitation of SPPs. Reproduced with permission from Pors *et al.*, Light Sci. Appl. **3**, e197 (2014). Copyright 2014 and licensed under a Creative Commons Attribution 3.0 Unported License.[32] (a) and (b) Measured SPP intensity distribution on the device surface under x- and y-polarized illumination, respectively. (c) Scanning electron microscopy (SEM) image of the metasurface. (d) and (e) Circular-polarization-dependent unidirectional excitation of SPPs. Reprinted with permission from Mühlenbernd *et al.*, ACS Photonics **3**, 124–129 (2016). Copyright 2016 American Chemical Society.[34] (d) Schematic illustration. (e) Measured output intensity distribution under LCP (A), linear (B), and RCP (C) illumination. (f) and (g) Circular-polarization-dependent coupling of incident light into two different plasmonic waveguides. Reprinted with permission from Chen *et al.*, Nano Lett. **23**, 3326–3333 (2023). Copyright 2023 American Chemical Society.[37] (f) Schematic illustration. (g) Measured (top) and simulated (bottom) field intensity distributions on the device surface under LCP (left) and RCP (right) illumination.

radiation. The gap-plasmon metasurface platform described earlier [Fig. 2(a)] is ideally suited for this task because it naturally supports SPPs propagating on the underlying metal surface in close proximity to the NP phase shifters. For example, Figs. 4(a)–4(c) show the linear-polarization-controlled excitation of SPPs at $\lambda = 1550$ nm in an Au/SiO_2/Au metasurface with rectangular NPs.[32] As illustrated by the simulation results of Fig. 2(b), the reflection phase for x-polarized light in this configuration can be tuned by varying the NP size along the x direction, L_x, while at the same time exhibiting a much weaker dependence on L_y (and vice versa for y-polarized light). These two geometrical parameters can therefore be used to independently control the reflection phase profiles $\varphi(x, y)$ imparted by the metasurface on the x and y polarization components, e.g., for the separate excitation of SPPs propagating along the x and y directions, respectively. This behavior is demonstrated in Figs. 4(a) and 4(b), where the field intensity of the excited SPPs is imaged by leakage radiation microscopy.

The circular-polarization-selective excitation of SPPs can similarly be achieved with metasurfaces based on the PB phase.[30,34] As an illustration, Fig. 4(d) shows an Au/MgF_2/Au gap-plasmon metasurface where all the NPs have the same rectangular shape and dimensions, but each NP is rotated relative to its preceding unit along the x direction by a fixed angle $\Delta\alpha$.[34] As a result, the metasurface introduces a linear reflection phase profile $\varphi(x, y) = \pm 2\Delta\alpha x/\Lambda$ (where Λ is the NP separation) for RCP and LCP light, respectively. The geometrical design parameters $\Delta\alpha$ and Λ are then selected so that the added wavevector $\nabla\varphi(x, y) = \pm 2\Delta\alpha\, \hat{\mathbf{x}}/\Lambda$ can couple the RCP and LCP components of normally incident light at $\lambda = 800$ nm into SPPs propagating, respectively, along the positive and negative x directions. The excited SPPs in this case are measured after conversion back into free-space radiation by nearby diffraction gratings [Fig. 4(e)]. A similar functionality has been demonstrated with y-oriented lines of identical rectangular nanoapertures perforated through an Au film,[31] which can scatter incident light into SPPs propagating along the positive and negative x directions. Using two adjacent lines of different nanoaperture orientations, the corresponding SPPs excited by RCP light can interfere constructively in the +x direction and destructively in the −x direction (and vice versa for the LCP-excited SPPs), leading to helicity-dependent unidirectional SPP launching. Both approaches can also be extended to enable wavefront shaping of the excited SPPs by varying the dimensions of the individual NPs or nanoapertures to encode an additional

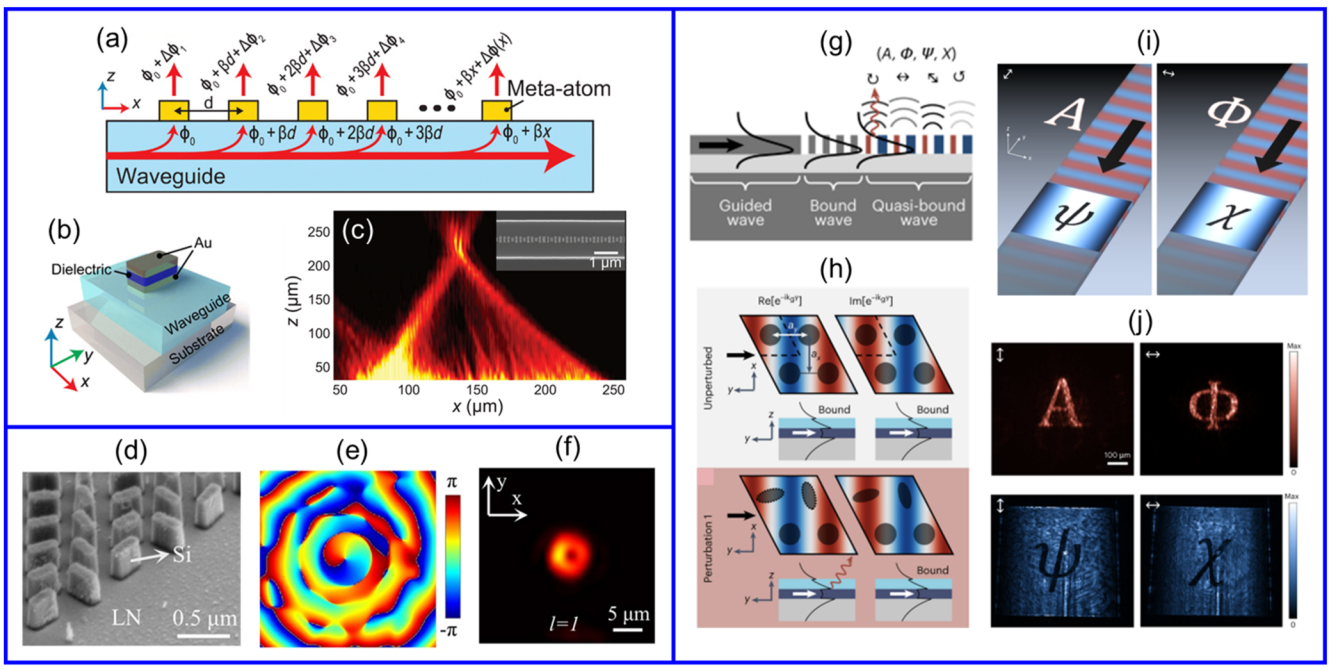

FIG. 5. Metasurface dielectric waveguide couplers. (a)–(c) Guided-wave-driven metasurfaces for complex free-space wavefront shaping. Reproduced with permission from Guo *et al.*, Sci. Adv. **6**, eabb4142 (2020). Copyright 2020 Authors, licensed under a Creative Commons Attribution NonCommercial License 4.0 (CC BY-NC).[44] (a) Schematic illustration. (b) Meta-atom geometry. (c) Measured field intensity profile on the x-z plane produced by a focusing metasurface (shown in the inset). (d)–(f) Geometric-phase metasurfaces for guided wave outcoupling. Reproduced with permission from Fang *et al.*, Nanophotonics **11**, 1923–1930 (2022). Copyright 2022 Authors, licensed under a Creative Commons Attribution 4.0 International License.[49] (d) SEM image. (e) FDTD-simulated phase profile imparted on the output light by a metasurface designed for the generation of a vortex beam. (f) Measured field intensity distribution produced by the same device on its focal plane. (g)–(j) Leaky-wave metasurfaces for the simultaneous shaping of phase, amplitude, and polarization. Reprinted with permission from Huang *et al.*, Nat. Nanotechnol. **18**, 580–588 (2023). Copyright 2023 Springer Nature.[50] (g) and (h) Side and top views of the basic device structure. The bottom panel of (h) shows possible perturbations applied to the unit cells to selectively couple the real field component of the guided light to free space. (i) Schematic illustration of a device designed to produce a four-image hologram encoded in the amplitudes (the letters ψ and χ) and phases (A and Φ) of two orthogonal polarizations (linear along x and y). (j) Polarized field intensity distributions measured with the same device at the image plane (top) and on the waveguide surface (bottom).

resonance phase profile Δφ(x, y) on the metasurface response.[33,35,37] One example is the Ag/SiO_2/Ag gap-plasmon metasurface pictured in Fig. 4(f), where the PB phase distribution again launches SPPs in opposite directions (±x) depending on the incident light helicity, while the resonance phase profile adds curvature to the SPP wavefronts on the x-y plane.[37] As a result, each excited SPP is focused toward the input of an on-chip hybrid plasmonic waveguide (loaded by a SiO_2 strip on the Ag surface). The NPs in this case are based on a connected double-arc geometry [inset of Fig. 4(f)], and their resonance phase is controlled by varying the angle subtended by each arc. Both experimental and numerical results, shown, respectively, in the upper and lower panels of Fig. 4(g), confirm the expected behavior at the design wavelength of 1064 nm.

Similar ideas have also been explored in the context of planar dielectric waveguides in a recent theoretical[40–43] and experimental[44–50] studies. These reports have mostly focused on converting a guided mode into free-space radiation emerging from the waveguide top surface with prescribed characteristics to implement functionalities such as collimation, focusing, OAM generation, and holography. A possible configuration is shown in Fig. 5(a), where the NPs are patterned on the top surface of the waveguide at a sufficiently small distance from the core to ensure significant overlap with the evanescent field of the guided mode. Each meta-atom, therefore, scatters a small portion of the guided light into free space with its designed phase shift, analogous to the operation of phased-array antennas. In Ref. 44, this approach was implemented with a periodic array of rectangular NPs of different dimensions, each consisting of an Au/SiO_2/Au sandwich structure [Fig. 5(b)], fabricated on a Si-on-insulator ridge waveguide. Here, the magnetic and electric dipole resonances of each meta-atom, excited by the fundamental TE mode of the waveguide, can combine to allow for the required 2π phase coverage. Multiple wavefront forming functionalities were demonstrated with this platform, including beam focusing as illustrated by the measured field intensity profile shown in Fig. 5(c). The meta-atoms on the waveguide top surface can also be designed based on the PB phase, as illustrated in Figs. 5(d)–5(f), where identical Si NPs of different orientations are patterned on a lithium-niobate-on-insulator ridge.[49] In this study, different metasurfaces were placed in series on the same waveguide to demonstrate multiple consecutive operations, including the generation of a vortex beam with nonzero OAM = $L\hbar$ per photon, which requires the additional phase profile $\Delta\varphi(x,y) = L\ \arctan(y/x)$ [Figs. 5(e) and 5(f)]. In addition to outcoupling of the guided modes into free space, various metasurfaces have also been employed in dielectric waveguides for controlled mode conversion,[51,52] asymmetric waveguiding,[53] and on-chip wavefront shaping.[54]

A conceptually different approach for interfacing guided light with free-space radiation has been introduced in Ref. 50, based on the notion of nonlocal metasurfaces,[55,56] which are designed to manipulate spatially extended modes supported by multiple diffractively coupled unit cells. In this approach, the waveguide is a photonic crystal slab consisting of a periodic array of cylindrical holes [Figs. 5(g) and 5(h), upper panel], where the dispersion of the guided modes defines the photonic band structure[15] (a tutorial review of the basic principles of photonic crystal slabs relevant to this discussion is presented in the supplementary material). In the outcoupler section of the waveguide, different holes are deformed into elliptical shapes of varying aspect ratios and orientations [Fig. 5(h), lower panel], designed to reduce the overall translational symmetry of the slab. These deformations produce a folding of the band diagram in the Brillouin zone of the perturbed crystal, which, in turn, converts some of the guided modes into quasi-bound states above the light line leaking into the radiation continuum. The amplitude, phase, and polarization of the outcoupled light can then be separately controlled in each unit cell by tuning its local perturbations. A full demonstration of this capability is shown in Figs. 5(i) and 5(j), where a Si_3N_4/polymer waveguide is used to generate a four-image hologram encoded in the amplitudes (the letters ψ and χ) and phases (A and Φ) of two orthogonal polarizations [linear along the x and y directions in the coordinate system of Fig. 5(h)].

IV. LIGHT EMITTERS

The distinct capabilities of phase gradient metasurfaces can also be leveraged to shape the output radiation of light emitting devices. This idea represents a powerful extension of two areas of significant prior study. The first is the control of spontaneous emission via modification of the local density of optical modes (or, equivalently, of the mode field distributions) through the Purcell effect;[57] i.e., the larger the normalized field intensity of a mode at the emitter location, the larger the spontaneous emission rate into that particular mode. This effect has been widely explored with several different platforms, including systems supporting surface waves,[58,59] micro- and nanocavities,[60] and nanoantennas.[61] The second area of related prior study is the use of periodically patterned nanostructures in the near-field vicinity of a light emitting layer to increase extraction efficiency and to control the directionality of the output radiation through diffractive effects.[62–64] The initial studies on (or leading to) metasurface-controlled light emission have extended this approach to periodic systems with asymmetric unit cells designed to produce anisotropic radiation patterns.[10,65–67]

Building on these ideas, a general theoretical description of light emission near a phase gradient metasurface has been presented in Ref. 68 [Fig. 6(a)]. This study considered a radiating dipole located at a subwavelength distance from a planar surface featuring a linear reflection phase profile φ(x, y) = ξx. The electric field generated by the dipole can be decomposed into a superposition of plane waves with different in-plane wavevectors **p**, including both radiative ($p < k_0 = 2\pi/\lambda$) and evanescent ($p > k_0$) components. Upon reflection from the metasurface, the wavevector of each plane wave is increased by the amount ξ in the x direction. As a result, some of the evanescent components of the emitted field [i.e., all the components within the blue regions in Fig. 6(a)] are scattered by the metasurface into radiative waves (within the red regions) and, therefore, contribute to the light output. Since this radiation mechanism is mediated by near-field interactions involving highly confined evanescent fields, it can be expected to occur with high probability and, therefore, dominate the dipole emission. Under these conditions, the far-field radiation pattern will therefore mostly consist of plane-wave components from within the red regions of Fig. 6(a), leading to directional emission. At the same time, the dipole spontaneous emission rate is also enhanced by the same interactions. In Ref. 68, these expectations were confirmed through rigorous FDTD simulations, revealing asymmetric radiation patterns and Purcell enhancement factors of up to several 100s depending on the metasurface phase gradient ξ.

A suitable reflective metasurface for the implementation of these ideas can be realized with the gap-plasmon platform. In this configuration, the metasurface directly supports highly confined guided waves (the SPPs at the underlying metal film) that introduce a resonance in the local density of optical modes. As a result, spontaneous emission by any nearby source is further modified through the preferential excitation of these SPPs at the expense of all other output channels (both radiative and evanescent). The far-field radiation pattern is then dominated by the SPP dispersion curve [blue line in Fig. 6(b)] shifted into the radiation cone by the metasurface phase gradient. This behavior has been measured with an $Au/SiO_2/Au$ gap-plasmon metasurface consisting of Au nanostripes of different widths, coated with an ensemble of CdTe/ZnS quantum dots emitting near $\lambda = 800$ nm suspended in a polymer solution [Figs. 6(c) and 6(d)].[69] Under optical pumping, the output radiation of this device was found to be highly directional [Fig. 6(e)] and linearly polarized on the x-z plane, despite the spatially incoherent and unpolarized nature of the intrinsic quantum-dot emission. This observed increase in spatial coherence of the emitted light can be explained with the following general argument:[70] whenever an SPP is excited by a localized emitter (in this case a quantum dot), the excitation is efficiently and coherently transferred by the SPP to all the nanostripes within its propagation length, whose scattered fields can therefore interfere with one another to produce beamed emission. By reciprocity, similar geometries can thus also be used for the directional control of photodetection, as illustrated in Sec. V below. In the study of Figs. 6(c)–6(e),[69] the x-polarized output power in the direction of peak emission was also found to be increased by a factor of about 4× relative to an identical sample without any metasurface, as a result of the underlying Purcell enhancement (partly offset by the SPP propagation losses in the Au film).

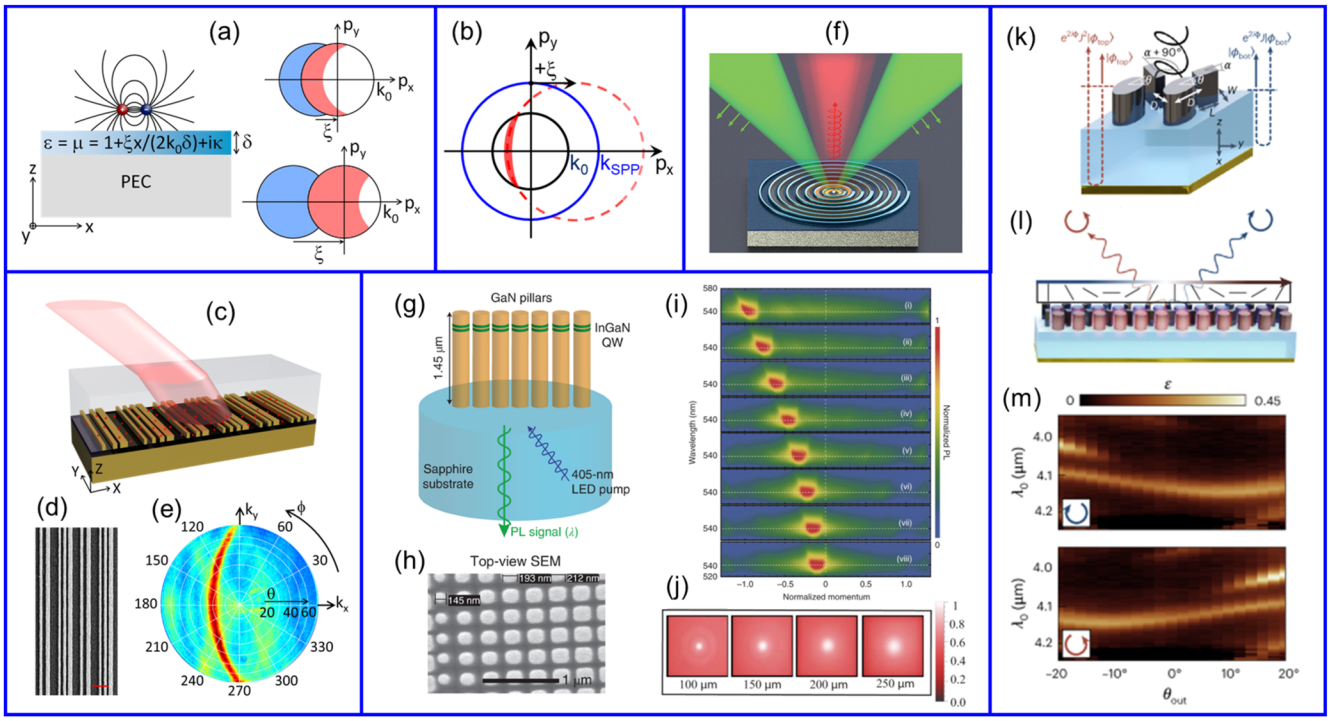

FIG. 6. Metasurface light emitting devices. (a) Theoretical model of light emission by a dipole source near a phase gradient metasurface. Reprinted with permission from Kogos and Paiella, ACS Photonics **3**, 243–248 (2016). Copyright 2016, American Chemical Society.[68] Left: Detailed geometry investigated in this model. Right: Distribution of the plane-wave components of the dipole field involved in the main radiation process for two different values of the metasurface phase gradient ξ. (b) Schematic illustration of SPP-mediated light emission near a gap-plasmon metasurface. (c)–(e) Directional light emission from a gap-plasmon metasurface. Reprinted with permission from Wang *et al.*, Adv. Opt. Mater. **8**, 1901951 (2020). Copyright 2020 John Wiley and Sons.[69] (c) Schematic illustration. (d) Top-view SEM image. (e) Measured x-polarized far-field radiation pattern of a device designed for peak emission at $\theta = -20°$. (f) Generation of circularly polarized single photons with a plasmonic metasurface. Reprinted with permission from Kan *et al.*, Adv. Mater. **32**, 1907832 (2020). Copyright 2020 John Wiley and Sons.[71] Schematic device illustration, including the radially polarized pump light (green) and the emitted single photons (red). (g)–(i) Directional light emission from a semiconductor metasurface. Reprinted with permission from Iyer *et al.*, Nat. Photonics **14**, 543–548 (2020). Copyright 2020, Springer Nature.[74] (g) Schematic illustration. (h) Top-view SEM image. (i) Measured p-polarized photoluminescence intensity as a function of wavelength and normalized in-plane momentum from eight metasurfaces of different phase gradients. (j) Measured field intensity distributions on different transverse planes from a device designed for focused light emission. Reproduced with permission from Mohtashami *et al.*, Nat. Commun. 12, **3591** (2021). Copyright 2021 Authors, licensed under a Creative Commons Attribution 4.0 License.[75] (k)–(m) Nonlocal metasurfaces for asymmetric polarization-selective thermal emission. Reprinted with permission from Nolen *et al.*, Nat. Nanotechnol. **19**, 1627–1634 (2024). Copyright 2024 Springer Nature.[80] (k) Meta-unit geometry. (l) Schematic illustration of a device providing bidirectional splitting of RCP and LCP light. (m) Measured polarization-resolved thermal emission from the same device vs wavelength and angle, showing the expected asymmetry.

Plasmon-assisted light emission in a similar platform has also been used to extract and collimate circularly polarized single photons at λ = 665 nm from a localized quantum emitter (a nitrogen-vacancy center in a nanodiamond crystal) [Fig. 6(f)].[71] Here, the metasurface consists of polymeric circular nanostripes centered about the emitter on an SiO_2-coated Ag substrate, with azimuthally varying widths. The emitter excites cylindrically diverging SPPs, which are then diffracted by the equally spaced concentric nanostripes into free space along the surface normal. At the same time, as a result of the varying nanostripe widths, the SPP components traveling along any two orthogonal directions (which have orthogonal in-plane electric fields) are scattered with a $\pm\pi/2$ relative phase difference, which endows the emitted light with circular polarization. With this approach, the directional emission of single photons with chirality >0.8 was demonstrated under illumination with a tightly focused radially polarized pump laser beam. Additional recent work on the use of metasurfaces to control the emission of single photons, as well as the generation of entangled photon pairs, is reviewed in Refs. 72 and 73.

Figures 6(g) and 6(h) show an all-dielectric metasurface designed for directional light emission from InGaN/GaN multiple quantum wells (the preeminent material systems of visible LEDs).[74] The quantum wells in this device are embedded in a GaN film patterned in a square periodic array of nanopillars, whose dimensions are varied along the horizontal (x) direction to produce a linear transmission phase profile with geometrically tunable slope ξ. P-polarized light emission from an unpatterned but otherwise identical film mostly excites modes with a fixed in-plane wavevector slightly larger than the free-space value k_0, which are trapped inside the device by total internal reflection and correspondingly feature enhanced local field intensity at the quantum-wells position. Similar to the SPPs of Fig. 6(b), these modes define a circle in reciprocal space. In the patterned device, similar modes are again preferentially excited and then simultaneously scattered by the periodic nanopillar array (which shifts the circle by all reciprocal lattice vectors) and by the metasurface phase gradient [which shifts the circle by ξ along the x direction, as in Fig. 6(b)]. The array period and phase gradient were selected to produce two radiative diffraction orders overlapping in reciprocal space within the light cone. The resulting asymmetric directional light emission is illustrated in Fig. 6(i), which shows the measured photoluminescence intensity as a function of in-plane wavevector k_x (horizontal axis) and wavelength λ (vertical axis) for eight different devices of different phase slope ξ (increasing from top to bottom). A large (130–250×) increase in air-coupled external quantum efficiency was also observed with the same devices compared to the unpatterned films, which was attributed to several factors, including increased pump light absorption, increased extraction efficiency, and increased radiative efficiency due to strain relaxation effects in the nanopillars.

The same platform has also been used to demonstrate focused (or collimated) light emission,[75] with the nanopillar dimensions designed to produce the phase profile of a lens (or axicon) in addition to the outcoupling linear phase gradient, now directed radially toward the array center point. It should be noted that, strictly speaking, this configuration only provides the targeted output wavefronts (focused or collimated on-axis) for light emitted radially from the same center point, whereas the device radiation output has contributions from all the pillars. Nevertheless, the desired functionalities were successfully demonstrated, as illustrated by the focused intensity profiles shown in Fig. 6(j) (albeit accompanied by a non-negligible background of unfocused light). In a more recent study,[76] a similar metasurface based on InAs quantum dots embedded in GaAs nanopillars was used to demonstrate ultrafast (subpicosecond) dynamic steering of the emitted light. In this device, all the nanopillars have the same dimensions, and the required linear phase profile for directional light emission was created by exploiting the carrier-induced refractive-index shift in semiconductor materials. Specifically, different carrier densities (and, therefore, different refractive indices) were produced in different nanopillars through the absorption of ultrafast light pulses featuring a sawtooth spatial intensity profile across the metasurface area. The emission angle could then be tuned dynamically by varying the gradient of this intensity profile in the pump light.

Extensive recent work has also focused on the use of nonlocal metasurfaces to control light emission.[77–80] As mentioned earlier, these structures are derived from photonic crystal slabs supporting quasi-bound states in the continuum (q-BICs).[55,56] A BIC is a slab-guided mode above the light line (i.e., with the same frequency and wavevector of a radiation mode in the surrounding media), which is nevertheless forbidden from escaping into the radiation continuum due to a complete symmetry mismatch.[81] By introducing suitable symmetry-breaking perturbations in the photonic-crystal unit cells, the same mode becomes a q-BIC that can leak into free space with a radiative Q factor that decreases quadratically with the strength of the perturbation.[82] In the presence of light emission within the slab, such a q-BIC can be preferentially excited (compared to all other modes coupled to free space) by virtue of its stronger spatial confinement and associated Purcell enhancement. The amplitude, phase, and polarization profiles of the resulting radiation output can then be tailored by using different perturbations in different unit cells, similar to the waveguide coupler of Ref. 50 described earlier. A particularly important feature of q-BICs for metasurface-controlled light emission is that they only exist at individual points in reciprocal space (often the Γ point, where the in-plane crystal wavevector is zero) as a result of the delicate symmetry requirements that enable their formation in the first place. Therefore, the same phase profile, determined by the metasurface design, can be expected for all the photons correspondingly radiated into free space. In contrast, all other platforms described so far in this section rely on multiple guided modes that span a circle in reciprocal space [as in Fig. 6(b)]. When coupled into radiation, light waves originating from different guided modes will therefore feature different phase gradients in addition to the metasurface imprint. This behavior is, for example, responsible for the multiple emission angles observed in Fig. 6(e), and a similar argument can be made for the background of unfocused light in Fig. 6(j). Therefore, nonlocal metasurfaces could, in principle, allow for more complex and precise wavefront control in light emission. At the same time, again due to the stringent q-BIC symmetry requirements, achromatic broadband operation with these nonlocal devices can be expected to be significantly limited.

A recent demonstration of this general approach is illustrated in Figs. 6(k)–6(m).[80] In this study, the metasurface consists of amorphous-Si pillars on a SiO_2-coated Au film, which is heated to 300 °C to produce strong thermal emission. The pillars are arranged on a rectangular lattice, where each unit cell contains two identical

rectangular NPs oriented perpendicular to each other and two elliptical NPs of equal orientation and eccentricity [Fig. 6(k)]. The resulting photonic crystal slab supports a Γ-point q-BIC with a radiative Q factor determined by the in-plane aspect ratio of the rectangular pillars and selected to achieve critical coupling for maximum emissivity. The eccentricity of the elliptical NPs provides the required birefringence for polarization control. Finally, the orientations of both rectangular and elliptical pillars can be tuned to vary the local phase and polarization of the light scattered in each unit cell from the q-BIC into free space. This platform was used to demonstrate the bidirectional emission (at equal and opposite angles) of various orthogonal states of polarization by introducing suitably chosen gradients in the local polarization across the metasurface to create the desired polarized interference patterns in the far field. For example, the schematic diagram of Fig. 6(l) and the experimental data of Fig. 6(m) (polarization-resolved emissivity vs wavelength and angle) illustrate the bidirectional splitting of RCP and LCP light, analogous to the Rashba effect in electronic systems.[83] In addition, the same study also reported the off-axis unidirectional thermal emission of a single state of circular polarization, achieved with an array of unit cells emitting the same polarization state but with a linearly graded phase shift. These functionalities expand on significant prior studies on chiral emission with gradient metasurfaces[77,79] as well as periodic arrays of NPs with suitably broken symmetry.[84–87] In the context of thermal radiation control, we should also mention the recent demonstrations of asymmetric beaming with a metagrating[88] and of broadband directional emission with an epsilon-near-zero multilayer metamaterial.[89]

Metasurfaces have also been integrated on the top surface of complete LED[90,91] or VCSEL[92–94] device structures. In these studies, unlike all devices of Fig. 6, the meta-atoms are far removed from the near field of the active layer and, therefore, cannot directly control the emission process through Purcell enhancement effects. As a result, the metasurface cannot, for example, be used to increase the radiative decay rate or to enforce the emission of any prescribed state of polarization from incoherent light sources. Instead, this configuration is more analogous to the use of metasurfaces as free-standing plates designed to shape the wavefronts of incident light, but with the important added advantage of increased miniaturization. For example, in the study displayed in Figs. 7(a)–7(d),[90] a dielectric metasurface is used to steer by a prescribed angle the output light of a visible (620 nm) GaP-based multiple-quantum-well LED. Here, the device active layer is embedded in a Fabry–Perot cavity consisting of a bottom Au film and a top SiO_2/TiO_2 Bragg reflector. This configuration increases the directionality (and, therefore, spatial coherence) of the Lambertian LED radiation pattern, whose incoherent nature would otherwise not allow for uniform shaping across the entire wavefront. Collimated emission at the desired off-axis angle (around 30°) is then achieved simply by adding a linear phase gradient, which is encoded in a square periodic array of cylindrical Si nanopillars of different diameters patterned on the device top surface. The resulting asymmetric far-field

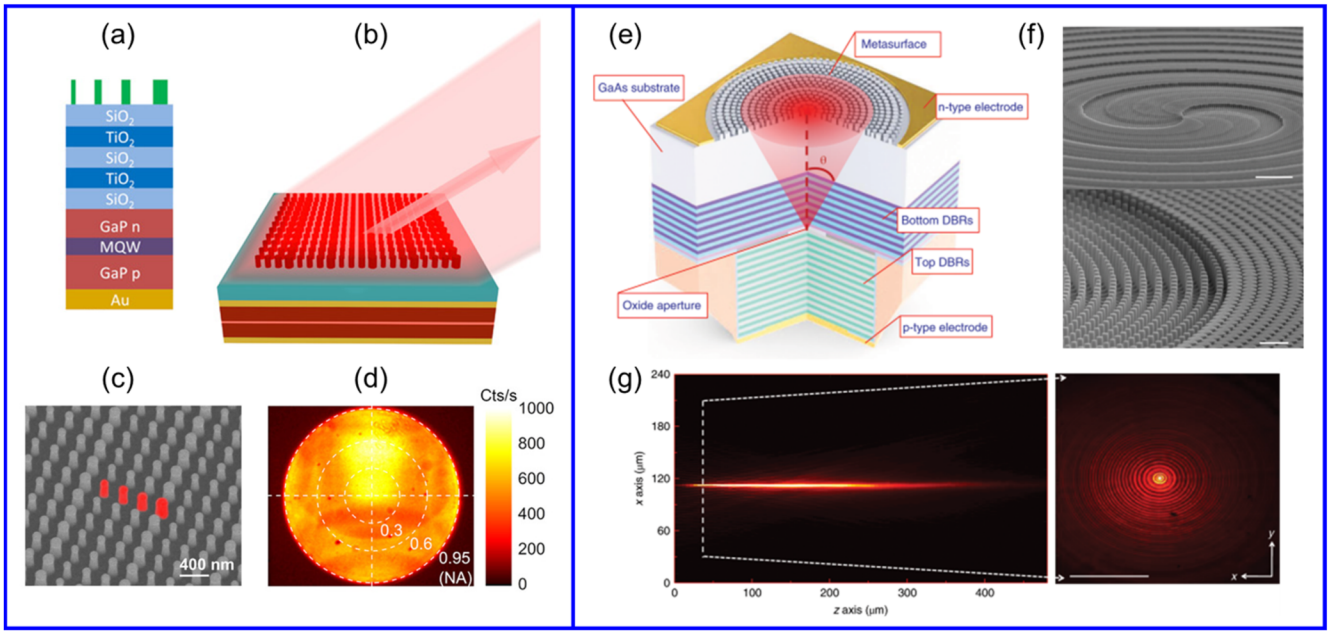

FIG. 7. Metasurfaces on LEDs and VCSELs. (a)–(d) Metasurface-integrated LED for directional light emission. Reprinted with permission from Khaidarov *et al.*, Laser Photonics Rev. **14**, 1900235 (2020). Copyright 2019 John Wiley and Sons.[90] (a) Side-view device geometry. (b) Schematic illustration of the device operation. (c) SEM image. (d) Measured far-field radiation pattern. (e)–(g) Metasurface-integrated GaAs VCSEL for beam shaping and collimation. Reprinted with permission from Xie *et al.*, Nat. Nanotechnol. **15**, 125–130 (2020). Copyright 2020 Springer Nature.[93] (e) Schematic device structure. (f) SEM images of a metasurface designed for vortex beam emission. The scale bars are 5 μm (top) and 500 nm (bottom). (g) Measured light intensity profile along the propagation axis (left) and on the transverse plane at z = 40 μm (right) of a non-diffractive Bessel beam generated with the same device platform.

radiation pattern, measured under optical pumping, is shown in Fig. 7(d).

Figures 7(e)–7(g) show a metasurface-integrated GaAs VCSEL emitting at 973 nm.[93] In this device, the laser beam reaches the top surface with a relatively large divergence angle, caused by diffraction through the narrow intra-cavity oxide aperture that is commonly used in VCSELs to enforce single-transverse-mode operation. At the same time, unlike the case of the LED just described, this beam still possesses a high degree of spatial coherence because it originates from stimulated emission. The metasurface, again consisting of cylindrical pillars of different diameters (in this case etched through the top GaAs layer), is then designed to collimate the output light and simultaneously shape its wavefronts. For example, Fig. 7(g) shows the measured intensity profile of a non-diffractive Bessel beam generated by combining the collimating phase profile with that of an axicon, which produces an assembly of tilted plane waves with wavevectors distributed on a cone. Importantly, these results were measured under current injection, with the metasurface found to have a negligible impact on the device's electrical characteristics and output power. In this respect, it should be noted that the other devices reviewed in this section are also potentially compatible with electrical pumping, although at the expense of increased structural complexity.

V. PHOTODETECTORS

Metasurfaces also hold great promise for the development of advanced multifunctional image sensors. Traditionally, photodetectors are designed to capture all the light impinging on their illumination window and convert it into an electrical signal proportional to its optical intensity. When combined in pixel arrays, these devices can therefore be used to map the intensity distribution of light waves incident from their surrounding objects for various imaging applications. At the same time, however, their basic operation principle does not allow for the direct detection of all the other properties of the incident light (phase, polarization, wavelength, OAM), which can also contain important information of interest. Instead, the measurement of these properties generally requires the use of complex and bulky optical systems (e.g., based on interferometry, polarimetry, or spectral or spatial filtering) that can substantially limit their widespread applicability. As a result, the development of more functional photodetectors capable of measuring multiple degrees of freedom simultaneously has recently emerged as a major research goal.[95,96] Within this general context, metasurfaces integrated on planar photodetectors could play a key enabling role by allowing for the selective detection of light incident with prescribed characteristics.

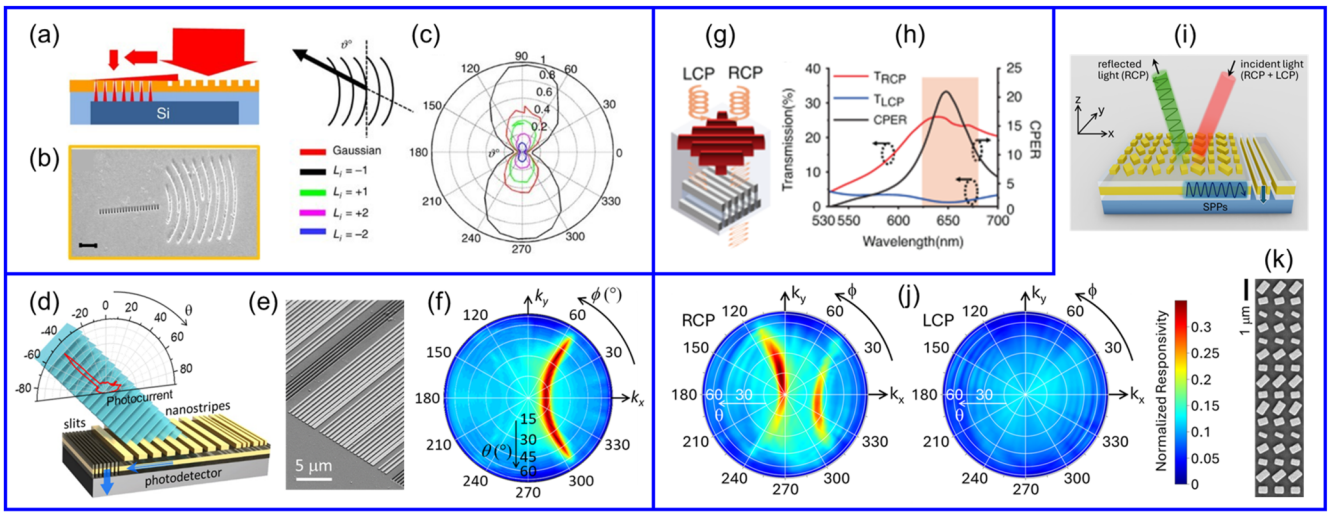

FIG. 8. Metasurface photodetectors. (a)–(c) Holographic metasurface couplers for OAM-selective photodetection. Reprinted with permission from Genevet *et al.*, Nat. Commun. **3**, 1278 (2012). Copyright 2012 Springer Nature.[99] (a) Schematic device structure. (b) Top-view SEM image of a coupler designed to detect incident light with topological charge L = −1. The scale bar is 1 μm. (c) Polarization-resolved photocurrent response of the same device under illumination with five beams of different topological charge. The polarization angle relative to the grooves is defined in the inset. (d)–(f) Angle-sensitive metasurface photodetectors. Reproduced with permission from Kogos *et al.*, Nat. Commun. **11**, 1637 (2020). Copyright 2020 Authors, licensed under a Creative Commons Attribution 4.0 International License.[100] [(d) and (f)]. (d) Schematic illustration and (inset) calculated angular response of a representative design. (e) SEM image. (f) Measured responsivity vs illumination angles from a device designed for peak photodetection at θ = 15°. (g) and (h) Chip-integrated metasurface full-Stokes polarimetric imaging system. Reproduced with permission from Zuo *et al.*, Light Sci. Appl. **12**, 218 (2023). Copyright 2023 Authors, licensed under a Creative Commons Attribution 4.0 International License.[111] (g) Schematic illustration of a single pixel designed to detect RCP light. (h) Measured transmission spectra and circular polarization extinction ratio (CPER) of the metasurface used in the same device. (i)–(k) Chiral metasurface photodetectors for circular-polarization-selective phase-contrast imaging. Reproduced with permission from Erturan *et al.*, Nanophotonics **14**, 947–957 (2025). Copyright 2025 Authors, licensed under a Creative Commons Attribution 4.0 International License.[116] (i) Schematic device structure. (j) Measured responsivity vs angles of incidence under RCP (left) and LCP (right) illumination for a device designed to detect the RCP phase gradient. (k) Top-view SEM images of the metasurface in the same device.

A particularly suitable configuration for this purpose is again the gap-plasmon metasurface, or any variation that similarly involves the phase- and/or polarization-matched excitation of SPPs on a metal film deposited on the device illumination window. In this configuration, any "undesired" incident light component (i.e., without the prescribed characteristics of interest) is automatically filtered out through reflection by the metal film. In contrast, the excited SPPs can be efficiently scattered into the underlying photodetector active layer with the use of subwavelength slits perforated through the metal film. The effectiveness of this process is well established in the context of extraordinary optical transmission:[97,98] when a SPP propagating on the top metal surface reaches the slit boundaries, a line of in-plane oscillating dipoles is effectively produced across the slit by the SPP electric field, which will then emit radiation propagating predominantly into the higher-index substrate. At the same time, the direct transmission of incoming radiation through apertures of subwavelength dimensions is negligibly small. An early demonstration of metasurface-controlled photodetection based on this idea is illustrated in Figs. 8(a)–8(c).[99] In this study, an Au film is deposited on a commercial Si photodiode and patterned with a curved diffraction grating of shallow grooves with a fork-like dislocation, positioned in front of an array of subwavelength holes. The grating is designed based on the principles of holography to couple an incident vortex beam with topological charge $L = -1$ (i.e., with each photon carrying an OAM of $-\hbar$) to SPPs converging toward the nanoholes. The resulting scattering of these SPPs into the Si substrate then leads to the preferential detection of the $L = -1$ vortex beam compared to any other type of incident wavefront. This behavior is illustrated by the polarization-resolved photocurrent data of Fig. 8(c), measured at a wavelength of 633 nm with various beams of different topological charge. The strong polarization dependence observed in the same figure is a consequence of the TM-polarized nature of SPPs, whereby their grating-coupled excitation is most efficient when the incident light is polarized perpendicular to the grating lines (i.e., parallel to the in-plane electric field of the excited SPPs).

A similar idea can be employed for angle-sensitive photodetection. In Ref. 100, this functionality was implemented with a periodic array of Au nanostripes on a $SiO_2/Au/SiO_2$ stack, surrounded on one side by a set of linear slits perforated through the stack and on the other side by a short gap-plasmon gradient-metasurface section consisting of Au nanostripes of different widths [Fig. 8(d)]. Light incident at the target detection angle [e.g., −45° in the simulations of Fig. 8(d)] is diffracted by the periodic array into SPPs that propagate toward the slits, where they are preferentially scattered into the underlying photodetector active layer. Light incident at the equal and opposite angle is diffracted into SPPs propagating toward the gradient-metasurface section, which is designed to scatter all incoming SPPs back into free space. Light incident along all other directions is simply reflected back by the metal film. Alternatively, a similar asymmetric angular response can be achieved with a single gap-plasmon metasurface providing a linear phase gradient, again combined with adjacent slits [Fig. 8(e)].[101] Figure 8(f) shows representative data (photocurrent vs illumination angles) measured in Ref. 100 with a metasurface-coated Ge photoconductor at 1550 nm. The curved region of high responsivity observed in this plot originates from the excitation of SPPs propagating along different directions [analogous to the radiation pattern of Fig. 6(e), which is based on a time-reversed version of the same process]. These angle-sensitive photodetectors are promising for multiple advanced imaging applications, including lensless compound-eye vision with an ultrawide field of view[100] and optical spatial filtering for image processing (based on the Fourier-optics correspondence between the spatial frequency components of an object and the transverse wavevectors of its scattered light).[102] Furthermore, similar devices can be used for the visualization of transparent phase objects through the measurement of small wavefront distortions if their target detection angle is sufficiently small so that the peak in their angular response overlaps asymmetrically with normal incidence.[103] This arrangement is analogous to phase imaging by oblique illumination[104] and can provide similar sensitivity (with state-of-the-art minimum detectable phase contrasts of a few mrad), but without the need for multiple illumination sources turned on sequentially, which can significantly limit speed and miniaturization.

The devices described in the preceding paragraphs can only detect light with linear polarization perpendicular to the metasurface grooves or nanostripes, again because of the TM character of SPPs. The selective detection of either state of circular polarization (RCP or LCP) is also of significant technological interest, motivated by applications such as chiral biochemical sensing,[105] quantum information processing,[106] and remote sensing.[107] Several devices providing this capability have been reported recently based on periodic (i.e., non-gradient) metasurfaces integrated on photodetectors.[108–114] For example, in the study displayed in Figs. 8(g) and 8(h),[111] a quarter-wave plate consisting of amorphous-Si nanograting lines is integrated vertically with a double-layer Al-nanowire linear polarizer. The quarter-wave-plate birefringence originates from the different degrees of optical confinement in the Si nanostripes experienced by light polarized along the stripe's long and short axes, as in the dielectric meta-atoms described earlier. The quarter-wave plate is oriented at ±45° with respect to the linear polarizer so that circularly polarized incident light is converted into linear polarization along the polarizer transmission or extinction axis, depending on its handedness. The resulting circularly polarized photodetection with high extinction ratio is illustrated in Fig. 8(h). The same study also reported full-Stokes polarimetric imaging with an array of these devices, combined on a silica plate in a checkerboard pattern with linear polarizers oriented along four different directions and integrated on a commercial CMOS image sensor by aligned UV bonding. Accurate reconstruction of the Stokes parameters was demonstrated with this highly miniaturized system, with measurement errors smaller than a few %, similar to state-of-the-art polarimeters involving bulky combinations of multiple photodetectors and/or reconfigurable wave plates.[115]

Angle-sensitive circularly polarized photodetection has also been reported in a more recent study [Figs. 8(i)–8(k)],[116] based on the general device architecture of Fig. 8(d). The gap-plasmon metasurface developed in this study consists of a square periodic array of rectangular Au NPs with different dimensions and orientations [Fig. 8(i)], selected to produce a linear profile in both resonance and PB phase along the same direction (x) and with the same slope in absolute value. As a result, for one circular polarization [RCP in Fig. 8(j)], depending on the sign of the NP relative orientations, these two phase profiles add up to each other to enable SPP-assisted directional photodetection through the nearby slits. At the same time, for the other circular polarization, the two phase distributions exactly

cancel each other so that light incident along any direction is simply reflected by the metasurface without any SPP excitation [right panel of Fig. 8(j)]. Interestingly, the curved regions of high responsivity in the RCP map of the same figure exhibit a strong asymmetry with respect to the horizontal axis, which can be explained in terms of spin conservation in photon/plasmon interactions[116] and, therefore, provides a direct illustration of spin-momentum locking in SPPs.[117] In the device of Fig. 8(j), the overall RCP phase gradient was designed to produce maximum responsivity at a small angle (about -2°) to enable phase imaging by wavefront sensing as described earlier. A pixel array of these photodetectors could therefore be used for the direct visualization of chiral birefringence.

Metasurfaces can also be employed to enhance the responsivity of thin-film photodetectors by steering the incident light at oblique angles to increase its propagation length through the active material and, therefore, its overall absorption. This idea has been demonstrated at visible wavelengths (560–690 nm) in an organic thin-film photodiode combined with an array of Au nanostripes of different widths embedded in ZnO, resulting in significant responsivity gains of up to over 2×.[118] The use of (periodic) plasmonic metasurfaces to increase the efficiency of photovoltaic solar cells has also been investigated extensively.[119] Finally, it should be mentioned that substantial recent work has also focused on the development of arrays of metasurfaces that could be integrated on standard image sensor arrays (with relatively thin spacer layers of prescribed thickness) to enable various functionalities such as polarimetry,[120,121] color routing,[122–124] and the measurement of angular momentum.[125] These devices are somewhere in between the fully integrated platforms of interest in the present tutorial and more traditional free-space metasurface components, in the sense that their design is more analogous to the latter (and largely decoupled from their intended optoelectronic interface), although they can offer a higher degree of system miniaturization.

VI. CONCLUSION AND OUTLOOK

The studies reviewed throughout this tutorial illustrate the ability of metasurfaces to enhance the functionality of waveguide couplers, light emitters, and photodetectors via direct integration, while at the same time providing a uniquely compact form factor. Specific capabilities demonstrated in these reports include the control of directionality, polarization, wavefront distribution, and OAM at the interface between free-space radiation and guided modes in photonic, plasmonic, and optoelectronic devices. In turn, these capabilities are of interest for multiple emerging technologies of great practical significance. One example is chip-to-chip optical interconnects that are becoming increasingly essential to address the bandwidth and power requirements of large-scale processing units and data centers. A key functionality for these systems is the efficient and versatile coupling of light in and out of complex photonic integrated circuits, particularly due to the lack of suitable on-chip Si light sources. Compared to standard solutions based on diffraction gratings, the superior design flexibility of metasurface waveguide couplers could provide significant advantages, e.g., increasing bandwidth and multiplexing capabilities. A second example is computer vision and image processing for applications ranging from autonomous navigation to biomedical microscopy. As briefly discussed in Sec. V, angle-sensitive photodetectors are particularly promising in this context because of their intrinsic optical spatial filtering capabilities, which could be exploited for edge enhancement (a key step for object classification with neural networks) and phase contrast imaging (e.g., to visualize transparent biological cells). Polarization vision is similarly attractive as a way to increase contrast under conditions of low visibility. Notably, integrated metasurface image sensors could enable these capabilities with unprecedented miniaturization and portability, which could dramatically expand their applicability. Finally, metasurface light emitters could find use in compact projectors for AR/VR headsets, again by virtue of their small dimensions and multifunctional operation.

To further advance the development of integrated metasurface devices for these applications, perhaps the main bottleneck at present is the demonstration of broadband achromatic operation. The ability to engineer spectral dispersion by geometrical design is, in fact, a key attribute of metasurface flat optics,[8] largely responsible for the recent progress toward the commercialization of free-space components such as the metalens. The design of broadband metasurfaces generally involves the use of complex building blocks with multiple geometrical degrees of freedom that allow enforcing the desired phase profiles at multiple wavelengths simultaneously (e.g., by controlling multiple resonances or by combining resonance and PB phase tuning). Similar ideas could be applied to enable broadband phase matching between free-space radiation of prescribed characteristics and waveguided modes with the type of metasurface devices described earlier. In turn, this capability would be particularly significant for applications involving waveguide coupling in photonic integrated circuits (again, to overcome the current bandwidth limitations of grating couplers) as well as image sensing under natural (and, therefore, broadband) illumination. Finally, a further leap in performance and technological potential could be achieved with the introduction of dynamic tunability in the metasurface phase and polarization response. This goal is currently the focus of extensive research across the entire field of metasurface flat optics, with several promising platforms being investigated, including gate-tunable conducting oxides, liquid crystals, phase-change materials such as GeSbTe, graphene, and MEMS/NEMS.[126] Due to their reliance on novel material systems and packaging architectures, these reconfigurable metasurfaces involve distinct fabrication processes and design principles, as well as additional performance metrics (including modulation speed and switching energy), all of which are presently being investigated in the context of free-space components. The adoption of similar platforms in integrated metasurface devices could open up new application prospects, for example, in LIDAR, dynamic displays, and lensless single-pixel imaging.

SUPPLEMENTARY MATERIAL

The supplementary material contains a tutorial description of the basic principles of photonic crystal slabs relevant to the nonlocal metasurfaces described in Secs. III and IV.

ACKNOWLEDGMENTS

The FDTD simulations presented in Fig. 2 were performed using the Shared Computing Cluster facility at Boston University. M.A.R. acknowledges support from the National Science Foundation under Grant No. ECCS-2139451.

AUTHOR DECLARATIONS

Conflict of Interest

The authors have no conflicts to disclose.

Author Contributions

Maliheh A. Roueini: Conceptualization (supporting); Formal analysis (lead); Writing – original draft (supporting). **Roberto Paiella**: Conceptualization (lead); Writing – original draft (lead).

DATA AVAILABILITY

The original data generated in this study (presented in Fig. 2) are available from the corresponding author upon reasonable request.

REFERENCES

[1]N. Yu and F. Capasso, "Flat optics with designer metasurfaces," Nat. Mater. **13**, 139–150 (2014).
[2]H. T. Chen, A. J. Taylor, and N. Yu, "A review of metasurfaces: Physics and applications," Rep. Prog. Phys. **79**, 076401 (2016).
[3]P. Genevet, F. Capasso, F. Aieta, M. Khorasaninejad, and R. Devlin, "Recent advances in planar optics: From plasmonic to dielectric metasurfaces," Optica **4**, 139 (2017).
[4]F. Ding, A. Pors, and S. I. Bozhevolnyi, "Gradient metasurfaces: A review of fundamentals and applications," Rep. Prog. Phys. **81**, 026401 (2018).
[5]S. M. Kamali, E. Arbabi, A. Arbabi, and A. Faraon, "A review of dielectric optical metasurfaces for wavefront control," Nanophotonics **7**, 1041–1068 (2018).
[6]A. Arbabi, Y. Horie, M. Bagheri, and A. Faraon, "Dielectric metasurfaces for complete control of phase and polarization with subwavelength spatial resolution and high transmission," Nat. Nanotechnol. **10**, 937–943 (2015).
[7]J. P. Balthasar Mueller, N. A. Rubin, R. C. Devlin, B. Groever, and F. Capasso, "Metasurface polarization optics: Independent phase control of arbitrary orthogonal states of polarization," Phys. Rev. Lett. **118**, 113901 (2017).
[8]W. T. Chen, A. Y. Zhu, and F. Capasso, "Flat optics with dispersion-engineered metasurfaces," Nat. Rev. Mater. **5**, 604–620 (2020).
[9]D. M. Pozar, S. D. Targonski, and H. D. Syrigos, "Design of millimeter wave microstrip reflectarrays," IEEE Trans. Antennas Propag. **45**, 287–296 (1997).
[10]A. Vaskin, R. Kolkowski, A. F. Koenderink, and I. Staude, "Light-emitting metasurfaces," Nanophotonics **8**, 1151–1198 (2019).
[11]Y. Meng, Y. Chen, L. Lu, Y. Ding, A. Cusano, J. A. Fan, Q. Hu, K. Wang, Z. Xie, Z. Liu, Y. Yang, Q. Liu, M. Gong, Q. Xiao, S. Sun, M. Zhang, X. Yuan, and X. Ni, "Optical meta-waveguides for integrated photonics and beyond," Light Sci. Appl. **10**, 235 (2021).
[12]R. Guan, H. Xu, Z. Lou, Z. Zhao, L. Wang, R. Guan, H. Xu, Z. Lou, L. Wang, and Z. Zhao, "Design and development of metasurface materials for enhancing photodetector properties," Adv. Sci. **11**, 2402530 (2024).
[13]X. Zhang, W. Li, F. Xie, K. Wang, G. Li, S. Liu, M. Wang, Z. Tang, and L. Zeng, "Metamaterials for high-performance photodetectors," Appl. Phys. Rev. **11**, 041316 (2024).
[14]S. T. Ha, Q. Li, J. K. W. Yang, H. V. Demir, M. L. Brongersma, and A. I. Kuznetsov, "Optoelectronic metadevices," Science **386**, eadm7442 (2024).
[15]W. Zhou and S. Fan, *Photonic Crystal Metasurface Optoelectronics* (Academic Press, 2019).
[16]W. Wang, M. Ramezani, A. I. Väkeväinen, P. Törmä, J. G. Rivas, and T. W. Odom, "The rich photonic world of plasmonic nanoparticle arrays," Mater. Today **21**, 303–314 (2018).
[17]F. Ding, Y. Yang, R. A. Deshpande, and S. I. Bozhevolnyi, "A review of gap-surface plasmon metasurfaces: Fundamentals and applications," Nanophotonics **7**, 1129–1156 (2018).
[18]S. Fan, W. Suh, and J. D. Joannopoulos, "Temporal coupled-mode theory for the Fano resonance in optical resonators," J. Opt. Soc. Am. A **20**, 569 (2003).
[19]M. Khorasaninejad and F. Capasso, "Broadband multifunctional efficient metagratings based on dielectric waveguide phase shifters," Nano Lett. **15**, 6709–6715 (2015).
[20]A. Arbabi, Y. Horie, A. J. Ball, M. Bagheri, and A. Faraon, "Subwavelength-thick lenses with high numerical apertures and large efficiency based on high-contrast transmitarrays," Nat. Commun. **6**, 7069 (2015).
[21]M. Decker, I. Staude, M. Falkner, J. Dominguez, D. N. Neshev, I. Brener, T. Pertsch, and Y. S. Kivshar, "High-efficiency dielectric Huygens' surfaces," Adv. Opt. Mater. **3**, 813–820 (2015).
[22]M. Chen, M. Kim, A. M. H. Wong, and G. V. Eleftheriades, "Huygens' metasurfaces from microwaves to optics: A review," Nanophotonics **7**, 1207–1231 (2018).
[23]L. Huang, X. Chen, H. Mühlenbernd, G. Li, B. Bai, Q. Tan, G. Jin, T. Zentgraf, and S. Zhang, "Dispersionless phase discontinuities for controlling light propagation," Nano Lett. **12**, 5750–5755 (2012).
[24]D. Lin, P. Fan, E. Hasman, and M. L. Brongersma, "Dielectric gradient metasurface optical elements," Science **345**, 298–302 (2014).
[25]A. C. Overvig, S. Shrestha, S. C. Malek, M. Lu, A. Stein, C. Zheng, and N. Yu, "Dielectric metasurfaces for complete and independent control of the optical amplitude and phase," Light Sci. Appl. **8**, 92 (2019).
[26]S. N. Khonina, N. L. Kazanskiy, and M. A. Butt, "Exploring diffractive optical elements and their potential in free space optics and imaging- A comprehensive review," Laser Photonics Rev. **18**, 2400377 (2024).
[27]Z. Li, R. Pestourie, Z. Lin, S. G. Johnson, and F. Capasso, "Empowering metasurfaces with inverse design: Principles and applications," ACS Photonics **9**, 2178–2192 (2022).
[28]W. Ji, J. Chang, H. X. Xu, J. R. Gao, S. Gröblacher, H. P. Urbach, and A. J. L. Adam, "Recent advances in metasurface design and quantum optics applications with machine learning, physics-informed neural networks, and topology optimization methods," Light Sci. Appl. **12**, 169 (2023).
[29]S. Sun, K. Y. Yang, C. M. Wang, T. K. Juan, W. T. Chen, C. Y. Liao, Q. He, S. Xiao, W. T. Kung, G. Y. Guo, L. Zhou, and D. P. Tsai, "High-efficiency broadband anomalous reflection by gradient meta-surfaces," Nano Lett. **12**, 6223–6229 (2012).
[30]L. Huang, X. Chen, B. Bai, Q. Tan, G. Jin, T. Zentgraf, and S. Zhang, "Helicity dependent directional surface plasmon polariton excitation using a metasurface with interfacial phase discontinuity," Light Sci. Appl. **2**, e70 (2013).
[31]J. Lin, J. P. B. Mueller, Q. Wang, G. Yuan, N. Antoniou, X. C. Yuan, and F. Capasso, "Polarization-controlled tunable directional coupling of surface plasmon polaritons," Science **340**, 331–334 (2013).
[32]A. Pors, M. G. Nielsen, T. Bernardin, J. C. Weeber, and S. I. Bozhevolnyi, "Efficient unidirectional polarization-controlled excitation of surface plasmon polaritons," Light Sci. Appl. **3**, e197 (2014).
[33]S.-Y. Lee, K. Kim, S.-J. Kim, H. Park, K.-Y. Kim, and B. Lee, "Plasmonic meta-slit: Shaping and controlling near-field focus," Optica **2**, 6 (2015).
[34]H. Mühlenbernd, P. Georgi, N. Pholchai, L. Huang, G. Li, S. Zhang, and T. Zentgraf, "Amplitude- and phase-controlled surface plasmon polariton excitation with metasurfaces," ACS Photonics **3**, 124–129 (2016).
[35]Q. Xu, X. Zhang, Y. Xu, C. Ouyang, Z. Tian, J. Gu, J. Li, S. Zhang, J. Han, and W. Zhang, "Polarization-controlled surface plasmon holography," Laser Photonics Rev. **11**, 1600212 (2017).
[36]C. Meng, S. Tang, F. Ding, and S. I. Bozhevolnyi, "Optical gap-surface plasmon metasurfaces for spin-controlled surface plasmon excitation and anomalous beam steering," ACS Photonics **7**, 1849–1856 (2020).
[37]Y. Chen, X. Zheng, X. Zhang, W. Pan, Z. Wang, S. Li, S. Dong, F. Liu, Q. He, L. Zhou, and S. Sun, "Efficient meta-couplers squeezing propagating light into on-chip subwavelength devices in a controllable way," Nano Lett. **23**, 3326–3333 (2023).
[38]J. N. Anker, W. P. Hall, O. Lyandres, N. C. Shah, J. Zhao, and R. P. Van Duyne, "Biosensing with plasmonic nanosensors," Nat. Mater. **7**, 442–453 (2008).
[39]Y. Fang and M. Sun, "Nanoplasmonic waveguides: Towards applications in integrated nanophotonic circuits," Light Sci. Appl. **4**, e294 (2015).

[40]Y. Zhang, Z. Li, W. Liu, Z. Li, H. Cheng, S. Chen, and J. Tian, "Spin-selective and wavelength-selective demultiplexing based on waveguide-integrated all-dielectric metasurfaces," Adv. Opt. Mater. **7**, 1801273 (2019).
[41]Y. Meng, Z. Liu, Z. Xie, R. Wang, T. Qi, F. Hu, H. Kim, Q. Xiao, X. Fu, Q. Wu, S.-H. Bae, M. Gong, and X. Yuan, "Versatile on-chip light coupling and (de)multiplexing from arbitrary polarizations to controlled waveguide modes using an integrated dielectric metasurface," Photonics Res. **8**, 564–576 (2020).
[42]C. Xie, L. Huang, W. Liu, W. Hong, J. Ding, W. Wu, and M. Guo, "Bifocal focusing and polarization demultiplexing by a guided wave-driven metasurface," Opt. Express **29**, 25709 (2021).
[43]Y. Ha, Y. Guo, M. Pu, X. Li, X. Ma, Z. Zhang, and X. Luo, "Monolithic-integrated multiplexed devices based on metasurface-driven guided waves," Adv. Theory Simul. **4**, 2000239 (2021).
[44]X. Guo, Y. Ding, X. Chen, Y. Duan, and X. Ni, "Molding free-space light with guided wave–driven metasurfaces," Sci. Adv. **6**, eabb4142 (2020).
[45]L. Li, K. Yao, Z. Wang, and Y. Liu, "Harnessing evanescent waves by bianisotropic metasurfaces," Laser Photonics Rev. **14**, 1900244 (2020).
[46]Y. Ding, X. Chen, Y. Duan, H. Huang, L. Zhang, S. Chang, X. Guo, and X. Ni, "Metasurface-dressed two-dimensional on-chip waveguide for free-space light field manipulation," ACS Photonics **9**, 398–404 (2022).
[47]R. Yang, S. Wan, Y. Shi, Z. Wang, J. Tang, and Z. Li, "Immersive tuning the guided waves for multifunctional on-chip metaoptics," Laser Photonics Rev. **16**, 2200127 (2022).
[48]Y. Shi, C. Wan, C. Dai, S. Wan, Y. Liu, C. Zhang, Z. Li, Z. Li, and Z. Li, "On-chip meta-optics for semi-transparent screen display in sync with AR projection," Optica **9**, 670–676 (2022).
[49]B. Fang, Z. Wang, S. Gao, S. Zhu, and T. Li, "Manipulating guided wave radiation with integrated geometric metasurface," Nanophotonics **11**, 1923–1930 (2022).
[50]H. Huang, A. C. Overvig, Y. Xu, S. C. Malek, C. C. Tsai, A. Alù, and N. Yu, "Leaky-wave metasurfaces for integrated photonics," Nat. Nanotechnol. **18**, 580–588 (2023).
[51]Z. Li, M. H. Kim, C. Wang, Z. Han, S. Shrestha, A. C. Overvig, M. Lu, A. Stein, A. M. Agarwal, M. Lončar, and N. Yu, "Controlling propagation and coupling of waveguide modes using phase-gradient metasurfaces," Nat. Nanotechnol. **12**, 675–683 (2017).
[52]C. Wu, H. Yu, S. Lee, R. Peng, I. Takeuchi, and M. Li, "Programmable phase-change metasurfaces on waveguides for multimode photonic convolutional neural network," Nat. Commun. **12**, 96 (2021).
[53]R. Wang, Q. Wu, W. Cai, Q. Zhang, H. Xiong, B. Zhang, J. Qi, J. Yao, and J. Xu, "Broadband on-chip terahertz asymmetric waveguiding via phase-gradient metasurface," ACS Photonics **6**, 1774–1779 (2019).
[54]Z. Wang, T. Li, A. Soman, D. Mao, T. Kananen, and T. Gu, "On-chip wavefront shaping with dielectric metasurface," Nat. Commun. **10**, 3547 (2019).
[55]A. C. Overvig, S. C. Malek, and N. Yu, "Multifunctional nonlocal metasurfaces," Phys. Rev. Lett. **125**, 017402 (2020).
[56]A. Overvig and A. Alù, "Diffractive nonlocal metasurfaces," Laser Photonics Rev. **16**, 2100633 (2022).
[57]E. M. Purcell, "Spontaneous emission probabilities at radio frequencies," Phys. Rev. **69**, 681 (1946).
[58]G. W. Ford and W. H. Weber, "Electromagnetic interactions of molecules with metal surfaces," Phys. Rep. **113**, 195–287 (1984).
[59]W. L. Barnes, "Fluorescence near interfaces: The role of photonic mode density," J. Mod. Opt. **45**, 661–699 (1998).
[60]S. Noda, M. Fujita, and T. Asano, "Spontaneous-emission control by photonic crystals and nanocavities," Nat. Photonics **1**, 449–458 (2007).
[61]L. Novotny and N. Van Hulst, "Antennas for light," Nat. Photonics **5**, 83–90 (2011).
[62]J. J. Greffet, R. Carminati, K. Joulain, J. P. Mulet, S. Mainguy, and Y. Chen, "Coherent emission of light by thermal sources," Nature **416**, 61–64 (2002).
[63]J. J. Wierer, A. David, and M. M. Megens, "III-nitride photonic-crystal light-emitting diodes with high extraction efficiency," Nat. Photonics **3**, 163–169 (2009).
[64]G. Lozano, G. Grzela, M. A. Verschuuren, M. Ramezani, and J. G. Rivas, "Tailor-made directional emission in nanoimprinted plasmonic-based light-emitting devices," Nanoscale **6**, 9223–9229 (2014).
[65]J. Dimaria, E. Dimakis, T. D. Moustakas, and R. Paiella, "Plasmonic off-axis unidirectional beaming of quantum-well luminescence," Appl. Phys. Lett. **103**, 251108 (2013).
[66]L. Langguth, A. H. Schokker, K. Guo, and A. F. Koenderink, "Plasmonic phase-gradient metasurface for spontaneous emission control," Phys. Rev. B **92**, 205401 (2015).
[67]S. Liu, A. Vaskin, S. Addamane, B. Leung, M. C. Tsai, Y. Yang, P. P. Vabishchevich, G. A. Keeler, G. Wang, X. He, Y. Kim, N. F. Hartmann, H. Htoon, S. K. Doorn, M. Zilk, T. Pertsch, G. Balakrishnan, M. B. Sinclair, I. Staude, and I. Brener, "Light-emitting metasurfaces: Simultaneous control of spontaneous emission and far-field radiation," Nano Lett. **18**, 6906–6914 (2018).
[68]L. C. Kogos and R. Paiella, "Light emission near a gradient metasurface," ACS Photonics **3**, 243–248 (2016).
[69]X. Wang, Y. Li, R. Toufanian, L. C. Kogos, A. M. Dennis, and R. Paiella, "Geometrically tunable beamed light emission from a quantum-dot ensemble near a gradient metasurface," Adv. Opt. Mater. **8**, 1901951 (2020).
[70]L. Shi, T. K. Hakala, H. T. Rekola, J. P. Martikainen, R. J. Moerland, and P. Törmä, "Spatial coherence properties of organic molecules coupled to plasmonic surface lattice resonances in the weak and strong coupling regimes," Phys. Rev. Lett. **112**, 153002 (2014).
[71]Y. Kan, S. K. H. Andersen, F. Ding, S. Kumar, C. Zhao, and S. I. Bozhevolnyi, "Metasurface-enabled generation of circularly polarized single photons," Adv. Mater. **32**, 1907832 (2020).
[72]Y. Kan and S. I. Bozhevolnyi, "Advances in metaphotonics empowered single photon emission," Adv. Opt. Mater. **11**, 2202759 (2023).
[73]J. Zhang and Y. Kivshar, "Quantum metaphotonics: Recent advances and perspective," APL Quantum **1**, 020902 (2024).
[74]P. P. Iyer, R. A. DeCrescent, Y. Mohtashami, G. Lheureux, N. A. Butakov, A. Alhassan, C. Weisbuch, S. Nakamura, S. P. DenBaars, and J. A. Schuller, "Unidirectional luminescence from InGaN/GaN quantum-well metasurfaces," Nat. Photonics **14**, 543–548 (2020).
[75]Y. Mohtashami, R. A. DeCrescent, L. K. Heki, P. P. Iyer, N. A. Butakov, M. S. Wong, A. Alhassan, W. J. Mitchell, S. Nakamura, S. P. DenBaars, and J. A. Schuller, "Light-emitting metalenses and meta-axicons for focusing and beaming of spontaneous emission," Nat. Commun. **12**, 3591 (2021).
[76]P. P. Iyer, N. Karl, S. Addamane, S. D. Gennaro, M. B. Sinclair, and I. Brener, "Sub-picosecond steering of ultrafast incoherent emission from semiconductor metasurfaces," Nat. Photonics **17**, 588–593 (2023).
[77]K. Rong, B. Wang, A. Reuven, E. Maguid, B. Cohn, V. Kleiner, S. Katznelson, E. Koren, and E. Hasman, "Photonic Rashba effect from quantum emitters mediated by a Berry-phase defective photonic crystal," Nat. Nanotechnol. **15**, 927–933 (2020).
[78]A. C. Overvig, S. A. Mann, and A. Alù, "Thermal metasurfaces: Complete emission control by combining local and nonlocal light-matter interactions," Phys. Rev. X **11**, 021050 (2021).
[79]Y. Chen, J. Feng, Y. Huang, W. Chen, R. Su, S. Ghosh, Y. Hou, Q. Xiong, and C. W. Qiu, "Compact spin-valley-locked perovskite emission," Nat. Mater. **22**, 1065–1070 (2023).
[80]J. R. Nolen, A. C. Overvig, M. Cotrufo, and A. Alù, "Local control of polarization and geometric phase in thermal metasurfaces," Nat. Nanotechnol. **19**, 1627–1634 (2024).
[81]C. W. Hsu, B. Zhen, A. D. Stone, J. D. Joannopoulos, and M. Soljačić, "Bound states in the continuum," Nat. Rev. Mater. **1**, 16048 (2016).
[82]K. Koshelev, S. Lepeshov, M. Liu, A. Bogdanov, and Y. Kivshar, "Asymmetric metasurfaces with high-Q resonances governed by bound states in the continuum," Phys. Rev. Lett. **121**, 193903 (2018).
[83]A. Manchon, H. C. Koo, J. Nitta, S. M. Frolov, and R. A. Duine, "New perspectives for Rashba spin–orbit coupling," Nat. Mater. **14**, 871–882 (2015).
[84]J. Wang, H. Li, Y. Ma, M. Zhao, W. Liu, B. Wang, S. Wu, X. Liu, L. Shi, T. Jiang, and J. Zi, "Routing valley exciton emission of a WS_2 monolayer via delocalized Bloch modes of in-plane inversion-symmetry-broken photonic crystal slabs," Light Sci. Appl. **9**, 148 (2020).
[85]X. Zhang, Y. Liu, J. Han, Y. Kivshar, and Q. Song, "Chiral emission from resonant metasurfaces," Science **377**, 1215–1218 (2022).

[86]X. Wang, T. Sentz, S. Bharadwaj, S. K. Ray, Y. Wang, D. Jiao, L. Qi, and Z. Jacob, "Observation of nonvanishing optical helicity in thermal radiation from symmetry-broken metasurfaces," Sci. Adv. **9**, eade4203 (2023).
[87]A. Nguyen, J.-P. Hugonin, A.-L. Coutrot, E. Garcia-Caurel, B. Vest, and J.-J. Greffet, "Large circular dichroism in the emission from an incandescent metasurface," Optica **10**, 232–238 (2023).
[88]J. Yu, R. Qin, Y. Ying, M. Qiu, and Q. Li, "Asymmetric directional control of thermal emission," Adv. Mater. **35**, 2302478 (2023).
[89]J. Xu, J. Mandal, and A. P. Raman, "Broadband directional control of thermal emission," Science **372**, 393–397 (2021).
[90]E. Khaidarov, Z. Liu, R. Paniagua-Domínguez, S. T. Ha, V. Valuckas, X. Liang, Y. Akimov, P. Bai, C. E. Png, H. V. Demir, and A. I. Kuznetsov, "Control of LED emission with functional dielectric metasurfaces," Laser Photonics Rev. **14**, 1900235 (2020).
[91]Y. Park, H. Kim, J. Y. Lee, W. Ko, K. Bae, and K. S. Cho, "Direction control of colloidal quantum dot emission using dielectric metasurfaces," Nanophotonics **9**, 1023–1030 (2020).
[92]M. S. Seghilani, M. Myara, M. Sellahi, L. Legratiet, I. Sagnes, G. Beaudoin, P. Lalanne, and A. Garnache, "Vortex laser based on III-V semiconductor metasurface: Direct generation of coherent Laguerre-Gauss modes carrying controlled orbital angular momentum," Sci. Rep. **6**, 38156 (2016).
[93]Y. Y. Xie, P. N. Ni, Q. H. Wang, Q. Kan, G. Briere, P. P. Chen, Z. Z. Zhao, A. Delga, H. R. Ren, H.-D. Chen, C. Xu, and P. Genevet, "Metasurface-integrated vertical cavity surface-emitting lasers for programmable directional lasing emissions," Nat. Nanotechnol. **15**, 125–130 (2020).
[94]P. Fu, P. N. Ni, B. Wu, X. Z. Pei, Q. H. Wang, P. P. Chen, C. Xu, Q. Kan, W. G. Chu, and Y. Y. Xie, "Metasurface enabled on-chip generation and manipulation of vector beams from vertical cavity surface-emitting lasers," Adv. Mater. **35**, 2204286 (2023).
[95]Y. Qu, S. Yi, L. Yang, and Z. Yu, "Multimodal light-sensing pixel arrays," Appl. Phys. Lett. **121**, 040501 (2022).
[96]S. Yuan, C. Ma, E. Fetaya, T. Mueller, D. Naveh, F. Zhang, and F. Xia, "Geometric deep optical sensing," Science **379**, eade1220 (2023).
[97]T. W. Ebbesen, H. J. Lezec, H. F. Ghaemi, T. Thio, and P. A. Wolff, "Extraordinary optical transmission through sub-wavelength hole arrays," Nature **391**, 667–669 (1998).
[98]J. Weiner, "The physics of light transmission through subwavelength apertures and aperture arrays," Rep. Prog. Phys. **72**(6), 064401 (2009).
[99]P. Genevet, J. Lin, M. A. Kats, and F. Capasso, "Holographic detection of the orbital angular momentum of light with plasmonic photodiodes," Nat. Commun. **3**, 1278 (2012).
[100]L. C. Kogos, Y. Li, J. Liu, Y. Li, L. Tian, and R. Paiella, "Plasmonic ommatidia for lensless compound-eye vision," Nat. Commun. **11**, 1637 (2020).
[101]J. Liu and R. Paiella, "Gradient-metasurface directional photodetectors," Opt. Lett. **49**(6), 1417 (2024).
[102]J. Liu, H. Wang, L. C. Kogos, Y. Li, Y. Li, L. Tian, and R. Paiella, "Optical spatial filtering with plasmonic directional image sensors," Opt. Express **30**, 29074–29087 (2022).
[103]J. Liu, H. Wang, Y. Li, L. Tian, and R. Paiella, "Asymmetric metasurface photodetectors for single-shot quantitative phase imaging," Nanophotonics **12**, 3519–3528 (2023).
[104]C. Bonati, T. Laforest, M. Kunzi, and C. Moser, "Phase sensitivity in differential phase contrast microscopy: Limits and strategies to improve it," Opt. Express **28**, 33767–33783 (2020).
[105]B. Ranjbar and P. Gill, "Circular dichroism techniques: Biomolecular and nanostructural analyses—A review," Chem. Biol. Drug Des. **74**, 101–120 (2009).
[106]E. Togan, Y. Chu, A. S. Trifonov, L. Jiang, J. Maze, L. Childress, M. V. G. Dutt, A. S. Sørensen, P. R. Hemmer, A. S. Zibrov, and M. D. Lukin, "Quantum entanglement between an optical photon and a solid-state spin qubit," Nature **466**, 730–734 (2010).
[107]J. S. Tyo, D. L. Goldstein, D. B. Chenault, and J. A. Shaw, "Review of passive imaging polarimetry for remote sensing applications," Appl. Opt. **45**, 5453–5469 (2006).
[108]W. Li, Z. J. Coppens, L. V. Besteiro, W. Wang, A. O. Govorov, and J. Valentine, "Circularly polarized light detection with hot electrons in chiral plasmonic metamaterials," Nat. Commun. **6**, 8379 (2015).
[109]M. Jung, S. Dutta-Gupta, N. Dabidian, I. Brener, M. Shcherbakov, and G. Shvets, "Polarimetry using graphene-integrated anisotropic metasurfaces," ACS Photonics **5**, 4283–4288 (2018).
[110]L. Li, J. Wang, L. Kang, W. Liu, L. Yu, B. Zheng, M. L. Brongersma, D. H. Werner, S. Lan, Y. Shi, Y. Xu, and X. Wang, "Monolithic full-Stokes near-infrared polarimetry with chiral plasmonic metasurface integrated graphene–silicon photodetector," ACS Nano **14**, 16634–16642 (2020).
[111]J. Zuo, J. Bai, S. Choi, A. Basiri, X. Chen, C. Wang, and Y. Yao, "Chip-integrated metasurface full-Stokes polarimetric imaging sensor," Light Sci. Appl. **12**, 218 (2023).
[112]J. Wei, Y. Chen, Y. Li, W. Li, J. Xie, C. Lee, K. S. Novoselov, and C. W. Qiu, "Geometric filterless photodetectors for mid-infrared spin light," Nat. Photonics **17**, 171–178 (2022).
[113]J. Hong, J. van de Groep, N. Lee, S. J. Kim, P. Lalanne, P. G. Kik, and M. L. Brongersma, "Nonlocal metasurface for circularly polarized light detection," Optica **10**, 134–141 (2023).
[114]G. Zhang, X. Lyu, Y. Qin, Y. Li, Z. Fan, X. Meng, Y. Cheng, Z. Cao, Y. Xu, D. Sun, Y. Gao, Q. Gong, and G. Lyu, "High discrimination ratio, broadband circularly polarized light photodetector using dielectric achiral nanostructures," Light Sci. Appl. **13**, 275 (2024).
[115]J. Li, H. Liu, Y. Zheng, J. Lei, Q. Zhao, Z. Xiong, R. Liao, and H. Ma, "Accurate and robust calibration method for simultaneous Stokes polarimetry," Measurement **223**, 113773 (2023).
[116]A. M. Erturan, J. Liu, M. A. Roueini, N. Malamug, L. Tian, and R. Paiella, "Chiral phase-imaging meta-sensors," Nanophotonics **14**, 947–957 (2025).
[117]K. Y. Bliokh, D. Smirnova, and F. Nori, "Quantum spin Hall effect of light," Science **348**, 1448–1451 (2015).
[118]X. Xu, H. Kwon, B. Gawlik, N. Mohammadi Estakhri, A. Alù, S. V. Sreenivasan, and A. Dodabalapur, "Enhanced photoresponse in metasurface-integrated organic photodetectors," Nano Lett. **18**, 3362–3367 (2018).
[119]H. A. Atwater and A. Polman, "Plasmonics for improved photovoltaic devices," Nat. Mater. **9**, 205–213 (2010).
[120]E. Arbabi, S. M. Kamali, A. Arbabi, and A. Faraon, "Full-Stokes imaging polarimetry using dielectric metasurfaces," ACS Photonics **5**, 3132–3140 (2018).
[121]Z. Yang, Z. Wang, Y. Wang, X. Feng, M. Zhao, Z. Wan, L. Zhu, J. Liu, Y. Huang, J. Xia, and M. Wegener, "Generalized Hartmann-Shack array of dielectric metalens sub-arrays for polarimetric beam profiling," Nat. Commun. **9**, 4607 (2018).
[122]B. H. Chen, P. C. Wu, V. C. Su, Y. C. Lai, C. H. Chu, I. C. Lee, J. W. Chen, Y. H. Chen, Y. C. Lan, C. H. Kuan, and D. P. Tsai, "GaN metalens for pixel-level full-color routing at visible light," Nano Lett. **17**, 6345–6352 (2017).
[123]M. Miyata, N. Nemoto, K. Shikama, F. Kobayashi, and T. Hashimoto, "Full-color-sorting metalenses for high-sensitivity image sensors," Optica **8**, 1596 (2021).
[124]X. Zou, Y. Zhang, R. Lin, G. Gong, S. Wang, S. Zhu, and Z. Wang, "Pixel-level Bayer-type colour router based on metasurfaces," Nat. Commun. **13**, 3288 (2022).
[125]J. Cheng, X. Sha, H. Zhang, Q. Chen, G. Qu, Q. Song, S. Yu, and S. Xiao, "Ultracompact orbital angular momentum sorter on a CMOS chip," Nano Lett. **22**, 3993–3999 (2022).
[126]J. Yang, S. Gurung, S. Bej, P. Ni, and H. W. Howard Lee, "Active optical metasurfaces: Comprehensive review on physics, mechanisms, and prospective applications," Rep. Prog. Phys. **85**, 036101 (2022).